

The origins of Calcium-rich supernovae from disruptions of CO white-dwarfs by hybrid He-CO white-dwarfs

YOSSEF ZENATI,^{1,2,*} HAGAI B. PERETS,² LUC DESSART,³ WYNN V. JACOBSON-GALÁN,⁴ SILVIA TOONEN,⁵ AND ARMIN REST^{6,1}

¹*Physics and Astronomy Department, Johns Hopkins University, Baltimore, MD 21218, USA*

²*Technion - Israel Institute of Technology, Physics department, Haifa Israel 3200002*

³*Institut d'Astrophysique de Paris, CNRS-Sorbonne Université, 98 bis boulevard Arago, F-75014 Paris, France*

⁴*Department of Astronomy and Astrophysics, University of California, Berkeley, CA 94720, USA*

⁵*Anton Pannekoek Institute for Astronomy, University of Amsterdam, 1090 GE Amsterdam, The Netherlands*

⁶*Space Telescope Science Institute, 3700 San Martin Dr., Baltimore, MD 21218, USA*

ABSTRACT

Calcium-rich explosions are very faint ($M_B \sim -15.5$), type I supernovae (SNe) showing strong Ca-lines, mostly observed in old stellar environments. Several models for such SNe had been explored and debated, but non were able to consistently reproduce the observed properties of Ca-rich SNe, nor their rates and host-galaxy distributions. Here we show that the disruptions of low-mass carbon-oxygen (CO) white dwarfs (WDs) by hybrid Helium-CO (HeCO) WDs during their merger could explain the origin and properties of such SNe. We make use of detailed multi-dimensional hydrodynamical-thermonuclear (FLASH) simulations to characterize such explosions. We find that the accretion of CO material onto a HeCO-WD heats its He-shell and eventually leads to its "weak" detonation and ejection and the production of a sub-energetic $\sim 10^{49}$ erg Ca-rich SN, while leaving the CO core of the HeCO-WD intact as a hot remnant WD, possibly giving rise to X-ray emission as it cools down. We model the detailed light-curve and spectra of such explosions to find an excellent agreement with observations of Ia/c Ca-rich might potentially also Ib Ca-rich SNe. We thereby provide a viable, consistent model for the origins of Ca-rich. These findings can shed new light on the role of Ca-rich in the chemical evolution of galaxies and the intra-cluster medium, and their contribution to the observed 511 keV signal in the Galaxy originating from positrons produced from ^{44}Ti decay. Finally, the origins of such SNe points to the key-role of HeCO WDs as SN progenitors, and their potential role as progenitors of other thermonuclear SNe including normal Ia.

Keywords: supernovae: supernovae — supernova dynamics — explosive nucleosynthesis — hydrodynamical simulations — white dwarfs

1. INTRODUCTION

The discovery of the type Ib (He-rich, hydrogen poor) SN 2005E in a remote position of an early type galaxy, where no evidence of star-forming regions were detected lead to the detailed study and characterization of a novel type of faint Ca-rich SNe (hereafter denoted CaSNe).

The ejected mass from such SNe was inferred to be low ($\lesssim 0.6M_\odot$) and they are typically found in old stellar environments; in addition their photometric and spectroscopic properties are peculiar and differ from typical type Ib SNe. The light curve (lc) of those typical Ca-rich are characterized by peak luminosity of -14 to -16.5 mag, with fast rise times $t_r \lesssim 15$ days (Perets et al. 2010; Kasliwal et al. 2012;

Jacobson-Galán et al. 2020a). These SNe showed strong CaII lines, leading to their original identification as Ca-rich ¹

Many of these faint SNe showed evidence for Helium lines and were identified as type Ib SNe (Perets et al. 2010), although later surveys identified faint, Ca-rich Ia/c SNe showing no clear He lines, suggesting a likely continuum of spectroscopic properties showing a range of events, from SN Ia-like features (Ca-Ia objects) to those with SN Ib/c-like features (Ca-Ib/c objects) at peak light (De et al. 2020).

Detection of such SNe is difficult, given their low-luminosity and rapid evolution. However, the inferred rates of such SNe are likely in the range of 5-20% of the normal type Ia SNe rates (Perets et al. 2010; Kasliwal et al. 2012; De et al.

Corresponding author: Yossef Zenati, Hagai B. Perets
yzenati1@jhu.edu, hperets@physics.technion.ac.il

* CHE Israel Excellence Fellowship

¹ Some studies suggested that these explosions do not in fact produce more Ca in abundance relative to O, and suggested to term such SNe as Ca-strong SNe, referring to the line strength. However, in the models shown here, a large fraction of the ejecta is composed of Ca, as originally suggested (Perets et al. 2010), and we therefore refer to these objects as Ca-rich SNe, as originally suggested.

2020). The demographics of their host galaxies differ from that of normal type Ia SNe. Normal type Ia SNe are inferred to have a delay time distribution favoring short delays, most of which exploding up to a Gyr following their stellar progenitors formation (Maoz et al. 2018). In contrast, the majority of Ca-rich SNe were observed in early type galaxies, and are generally observed in old environments, far from star-forming regions (Perets et al. 2010, 2011a; Kasliwal et al. 2012; Lyman et al. 2013; De et al. 2020), suggesting a much more extended delay time distribution. Ca-rich SNe also appear to have a relatively large offsets from their host galaxy nuclei (Perets et al. 2010; Kasliwal et al. 2010; Foley 2015; De et al. 2020), however, this was shown to be the result of their high frequency in early type galaxies, which stellar halos are large (Perets & Beniamini 2021).

The recent discovery and detailed observations of a close by SN 2019ehk in M100 (De et al. 2021; Nakaoka et al. 2021), shed new light on the properties of such Ca-rich SNe, and in particular gave rise to the first detection of early X-ray emission from a thermonuclear SN (Jacobson-Galán et al. 2020a, 2021).

Given these various properties showing evidence for (I) large He abundances (either directly observed, or potentially inferred from the large abundance of He-burning intermediate element products), (2) inefficient burning, leading to low production of ^{56}Ni and faint, low luminosity SNe, and (III) old environments, we suggested that these SNe form a novel type of SNe, arising from thermonuclear explosions of He-rich WDs (Perets et al. 2010), rather than from the core-collapse of massive stars (typically thought to be the progenitors of type Ib SNe).

Production of faint and Ca-rich SNe in models were already seen in the 1980s (Woosley et al. 1986), were such SNe were produced in models of detonation of a He-shell (suggested to be accreted from a companion through stable mass-transfer) on CO WDs, which failed to explode the CO-WD. These did not receive much attention as they did not produce normal type Ia SNe, nor any other type of SNe observed at the time. More recent studies further explored these models, and termed such SNe .Ia SNe (Bildsten et al. 2007). Following our identification and characterization of Ca-rich arising from He-rich WD explosions, several models tried to reproduce the properties of Ca-rich SNe. These models explored the detonation of a massive He-shell on top of low-mass CO WDs (Shen et al. 2010; Waldman et al. 2011). Although such models did produce faint and Ca-rich SNe they produced light curves and spectral series were inconsistent with the observed evolution of Ca-rich SNe. Other scenarios such as a WD disrupted by a neutron star (NS) or a black hole (BH) typically produced too faint and too rapid evolving SNe, not resembling Ca-rich SNe (Metzger 2012; Fernández & Metzger 2013; MacLeod et al. 2014; Zenati et al. 2019a, 2020a; Bobrick et al. 2021). Classically study in the later stage of NS-He WD binaries, those may observed as ultracompact X-ray binaries (UCXBs) (Nelson et al. 1986; Chen et al. 2022). Furthermore, population synthesis models of NS-WD mergers did not produce significant long delay time distributions that could be consis-

tent with the significant fraction of early type host galaxies for Ca-rich SNe (Toonen et al. 2018).

We have already proposed earlier (Perets et al. 2019) that hybrid HeCO WDs (Iben & Tutukov 1985; Han et al. 2007; Prada Moroni & Straniero 2009; Zenati et al. 2019b) play a key role in the production of thermonuclear SNe (Perets et al. 2019; Pakmor et al. 2021), and may produce most of the normal type Ia SNe (Perets et al. 2019). Here we propose a novel model for the origins of Ca-rich SNe, in which a hybrid HeCO WD disrupts a low-mass CO-WD. The debris dynamically accrete on the hybrid WD, and then the CO debris mixes with the He-shell of the hybrid, and detonates, while the hybrid WD core does not explode. We show that such scenario can reproduce the overall light curve and spectra of Ca-rich SNe. We also find large abundances of Ca and ^{44}Ti are produced. As we also discuss elsewhere, the progenitors of such disruptions give rise to a significant population of SNe with long delay times that would be observed in early type host galaxies as observed for Ca-rich SNe (Toonen et al., in prep.).

This paper is organized as follows. In Section 2 we overview the proposed scenario and its basic aspects. We then present the initial conditions and structure of the post-disruption debris disk in our models 3. In the methods section 4 we present the details of our numerical results, including the FLASH axisymmetric hydro-thermonuclear simulations and the radiative transfer modeling. In Section 5 we present the disk evolution and explosion seen in our models, and the resulting light curves and spectra. We then discuss (section 6) our results in comparisons with observations, explore their implications, and point to potential caveats. In Section 7 briefly shows the stellar populations of Ca-rich followed by our summary 8.

2. DISRUPTION OF A CO-WD BY A HECO WD

Hybrid HeCO WDs (Iben & Tutukov 1985; Han et al. 2007; Prada Moroni & Straniero 2009; Zenati et al. 2019b) are formed in interacting binaries where an evolved red-giant is stripped of its hydrogen (mostly) and partly stripping of helium-rich envelope during its evolution. This complex binary evolution channel can give rise to hybrid-WDs, composed of significant fractions of both CO and He. Such hybrid WDs reside in the mass range of $\sim 0.4 - 0.73 M_{\odot}$ and contain a He-envelope containing $\sim 2 - 20\%$ of the WD-mass (Zenati et al. 2019b), with lower mass hybrids typically containing larger He fractions (but other HeCO formation branches might produce larger He fractions even in the high mass range; Pakmor et al. 2021). Such hybrid-WDs are frequent among compact WD-WD binaries that inspiral and merge in a Hubble-time; where 25% of all WD-WD mergers may include a HeCO-WD (Perets et al. 2019).

In a previous study we explored the case of a CO WDs of $> 0.7 M_{\odot}$ disrupting lower mass HeCO WDs, and eventually producing normal type Ia SNe (Perets et al. 2019). Here we investigate the cases where low-mass CO-WDs are disrupted by hybrid HeCO-WDs, and show that these lead to the

Table 1. Simulation Suite

Model	M_c	M_d	α	$R_{d,0}$	$t_{\text{visc},0}^{(a)}$
-	(M_\odot)	(M_\odot)	-	(cm)	(s)
fca ₁	0.63	0.55	0.1	2.08×10^9	53.2
fca ₂	0.63	0.52	0.1	2.2×10^9	61.8
fca ₃	0.58	0.52	0.1	2.1×10^9	50.1
fca ₄	0.63	0.55	0.05	2.08×10^9	106.4

Notes: ^(a) Calculated from Eq. (5), assuming a disk aspect ratio $\theta = 0.8$. Model fca₄ was not studied with tracer particles.

production of Ca-rich SNe with detailed properties matching those of observed Ca-rich SNe.

In the current models we do not simulate the actual disruption of the lower-mass WD, which require an expensive and less resolved 3D simulations, but assume, similar to (Perets et al. 2019) that it was already disrupted and formed a debris disk around the higher mass WD. The axisymmetric disk now allows us to use a 2D model. We therefore introduce a disk of debris around a HeCO in a 2D axis-symmetric simulation and follow the accretion evolution of the debris onto the embedded HeCO WD. As discussed below, the accreted material eventually heats up and a He-enriched detonation ensues in the outer shell of the HeCO WD, leading to a weak explosion, which leaves the core of HeCO WD intact. We then model the light-curve and spectra produced from the explosion using a non-LTE 1D code CMFGEN. In the following we discuss the various assumptions and modeling processes in more detail.

3. INITIAL CONDITIONS OF THE POST-DISRUPTION DEBRIS DISK

3.1. Disk structure

We focus on disks that form when a CO WD is tidally disrupted by a more massive HeCO-WD companion in a close binary system, and follow similar modeling of debris disk evolution around compact objects as done by us and others in other contexts (See, Papaloizou & Pringle 1984; Fryer et al. 1999; Metzger 2012; Fernández & Metzger 2013; Bobrick et al. 2017; Zenati et al. 2019a; Perets et al. 2019; Metzger et al. 2021). In this section we estimate the characteristic properties of these binary mergers analytically, and provide insights onto the initial conditions of the debris disk, the transient WD accretion phase, and the key timescales involved. We use these analytic results to establish the initial conditions for our numerical simulations described in Section 4.

3.1.1. Disk Formation

The disruption process of the companion WD depends on the stability of the mass loss following the onset of Roche lobe overflow (RLOF). Mass transfer occurs as the binary loses orbital angular momentum, resulting in RLOF of the secondary onto the primary. We are interested in the fate of unstable mass transfer in a binary system consisting of a

HeCO WD primary of mass M_{WD} and radius R_{WD} orbited by a secondary CO WD companion of mass $M_{\text{WD,CO}} \lesssim M_{\text{WD,HeCO}}$ and radius $R_{\text{WD,HeCO}} \gtrsim R_{\text{WD,CO}}$.

The characteristic radial dimension of the disk can be estimated as (e.g., Margalit & Metzger 2016)

$$R_{d,0} = a_{\text{RLOF}}(1+q)^{-1}. \quad (1)$$

The mass of the formed disk will be about equal to the original CO-WD, $M_{d,0} \approx M_{\text{WD}}^{\text{CO}}$. The stability of the mass-transfer depends on the mass ratio of the binary $q = \frac{M_{\text{WD}}^{\text{CO}}}{M_{\text{WD}}^{\text{HeCO}}} = 0.83 - 0.88$. For circular orbits, this takes place at an orbital separation (Eggleton 1983)

$$a_{\text{RLOF}} \approx R_{\text{WD}}^{\text{HeCO}} \frac{0.6q^{2/3} + \ln(1+q^{1/3})}{0.49q^{2/3}}, \quad (2)$$

These provide us with the typical masses and scales of the formed disks. Following the disruption, the newly formed disk is very thick, as also seen in 3D models of the disruption stage. The vertical scale-height H_0 and aspect ratio are typically $\theta_0 \equiv H_0/R_{d,0} \sim 0.55 - 0.9$ (Metzger 2012; Margalit & Metzger 2016; Zenati et al. 2019a; Metzger et al. 2021). The gravity pressure is $P_* \approx \rho c_s^2 \approx \Sigma/2\pi h$ where Σ is the initial surface density of the disk and c_s is the sound speed.

3.1.2. Disk stability

The formed disk evolves through accretion onto the central object, during which the disk heats up. Magnetic torques arising from the magneto-rotational instability (MRI; Balbus & Hawley 1998) likely transfer angular momentum of the material outward in the accretion disk so that material inspirals into the central object (in this study the HeCO WD). Our model does not include magnetic fields, and can not self-consistently introduce viscous evolution to the disk. Instead, the viscous evolution is modelled through the use of artificial viscosity, following a Shakura-Sunyaev-like viscous evolution. In principle gravitational instabilities might produce spiral arms in the the disk and provide other angular momentum transfer processes. However, the disk is likely to be stable. The Toomre (1964) stability parameter, Q , is given by

$$Q = \frac{\Omega c_s}{\pi G \Sigma} \Big|_{r=R_{d,0}} \approx \frac{(M_{\text{WD}}^{\text{HeCO}} + M_{\text{WD}}^{\text{CO}})^2}{M_{\text{WD}}^{\text{HeCO}} M_{\text{WD}}^{\text{CO}}} \frac{H_0}{a_{\text{RLOF}}} \sim \frac{1+q}{q} \theta. \quad (3)$$

For the typical disks masses and thickness we consider here, $\theta_0 = 0.55$ and $q \gtrsim 0.83 - 0.88$ $Q = 1.17 - 1.23$, and the disk is stable. Generally, during the following evolution of the disk the viscous heating is larger than the radiative cooling, and the disk is likely to be gravitationally stable up to the point a detonation occurs. This should nevertheless be further verified in future 3D simulations. Here, using 2D simulations we assume only viscous evolution; and postpone studies of other scenarios to future 3D models. In the following we briefly describe the overall timescales and accretion rates in

this process, and then discuss the numerical hydrodynamical modeling in the next sections.

Let us consider the relevant timescales which will later refer to. t_{orb} is orbital time-scale,

$$t_{orb} \simeq 42 \left(\frac{R_{d,0}}{R_{HeCO}} \right)^{3/2} \left(\frac{M_{d,0}}{M_{\odot}} \right)^{-1/2} s, \quad (4)$$

The viscous timescale is given by

$$t_{visc,0} \sim \frac{r^2}{\nu} \Big|_{R_{d,0}} \sim \frac{1}{\alpha} \frac{1}{\theta_0^2} \left(\frac{R_{d,0}^3}{GM_{WD}^{HeCO}} \right)^{1/2} s, \quad (5)$$

where $\nu = \alpha c_s H = \alpha r^2 \Omega_K \theta^2$ is the effective kinematic viscosity, $\Omega_K \equiv (GM_{d,0}/r^3)^{1/2}$ is the Keplerian orbital frequency, $c_s \approx H\Omega_K$ is the midplane sound speed, and α parameterizes the disk viscosity (see also sub-section 4.1).

The viscous accretion results in a characteristic accretion rate following (Shakura & Sunyaev 1973), where the characteristic peak accretion rate is approximately,

$$\dot{M}_0 \sim \frac{M_{d,0}}{t_{visc,0}} \sim 0.1 M_{\odot}, \alpha=0.1. \quad (6)$$

The timescale for photons to diffuse out of the disk midplane is then,

$$t_{diff} \simeq \kappa_{es} \frac{\Sigma}{\sqrt{2\pi}} H_0 \simeq 1 - 7 \times 10^5 yr, \quad (7)$$

and is typically longer than the other timescales, such that radiative cooling does not play an important role.

We therefore consider a stable accretion disk around the primary HeCO WD, and follow its evolution through 2D hydrodynamical simulations as we discuss below.

3.2. Disk structure

The initial disk model can be calculated using energy and pressure considerations. The total energy in the disk is given by the combined contribution from the gravitational, thermal and kinetic energy, $e_{tot} = E_{thermal} + E_{kinetic+rotation} + E_{gravity}$, given by

$$e_{tot} = \frac{1}{2} [v_{\bar{\rho}}^2 + \frac{l_z^2}{\bar{\rho}^2}] - \frac{GM_{d,0}}{r} - E_g(r, \rho) + e_{int}. \quad (8)$$

The maximum density ρ_{max} and temperature T_{max} are expected at the initial innermost part of the disk, R_0 , (in the midplane $z = 0$). At that position the pressure gradient must vanish:

$$\nabla p = 0 \quad \text{at} \quad \bar{\rho} = R_0, \quad (9)$$

where $p = p(\rho, T, X_i)$ is determined either using an ideal gas plus radiation or the Helmholtz EOS.

Our solution of the disk geometry depend on the EOS and the equilibrium for the fluid which is dominant by HeCO WD

potential ϕ_c , the centrifugal forces, and the specific angular momentum (Papaloizou & Pringle 1984).

$$-\frac{1}{\rho} \nabla P - \nabla \phi_c + \Omega^2 \bar{\rho} \hat{\rho} = 0. \quad (10)$$

By combining the above equation with equation (9) and the EOS, we can deduce the general equation (10) following (Stone et al. 1999), see also (Fernández & Metzger 2013) and (Zenati et al. 2019a),

$$\frac{P}{\rho} = \frac{(\gamma + 1)GM_c}{\gamma R_0} \left[\frac{R_0}{r} - \frac{1}{2} \left(\frac{R_0}{r \sin \theta} \right)^2 - \frac{1}{2d} \right]. \quad (11)$$

We can then use the conditions (8) and (9), and the temperature corresponding to $\frac{\gamma \mathfrak{R}_g T}{M_{d,0}} = \frac{GM_c}{R_0}$, where \mathfrak{R}_g is the gas constant. In addition we can solve for T_{max} and ρ_{max} . Following Stone et al. (1999) we normalize the torus density by ρ_{max} from 8 and 9, resulting in the density distribution

$$\frac{\rho}{\rho_{max}} = \left\{ \frac{2d}{d-1} \left[\frac{R_0}{r} - \frac{1}{2} \left(\frac{R_0}{r \sin \theta} \right)^2 - \frac{1}{2d} \right] \right\}^{\frac{1}{\gamma-1}}. \quad (12)$$

where d is the torus distortion parameter which is related to the internal energy at R_0 by

$$e_{int,max} = \frac{GM_{HeCO}}{R_0} \frac{1}{2\gamma} \frac{d-1}{d}. \quad (13)$$

Bounded torus configurations require distortion parameter $d > 1$. Imposing the requirement $d > 1$ for physical solutions, one can obtain d from the condition (13) using T_{max} and ρ_{max} from 8 and 9. Here, we set $\gamma = 5/3$ as an initial value, and then use iterative computations of the effective adiabatic index using the Helmholtz EOS, until a steady configurations is achieved.

Equipped with the initial disk structure, we can now explore the evolution of the disk and its explosive outcomes.

4. METHODS

We model the evolution of the debris disk through a 2D thermonuclear-hydrodynamical modelling using the FLASH open code (Fryxell et al. 2000), with a 19 elements nuclear network. The initial properties of the WDs and the disk compositions are calculated from stellar evolution 1D models of HeCO WDs (Zenati et al. 2019b) which are mapped into 2D in FLASH. We post-process the results from the explosions through a larger nuclear network using the TORCH code (Timmes & Swesty 2000a) in MESA (Paxton et al. 2015). We then make use of the non - local thermodynamic equilibrium (non-LTE) radiative transfer code CMFGEN (Hillier & Dessart 2012) to model the light-curve and spectra arising from the modelled explosions, which we then compare to the observations. These various steps are discussed in more detail below.

The nature of our FLASH simulations is similar to those we ran earlier in other WD (or neutron star/black-hole) +

disk configurations, and are described in (Zenati et al. 2019a; Perets et al. 2019; Zenati et al. 2020a,b; Bobrick et al. 2021; Metzger et al. 2021). However, the type and masses of the WDs involved and their compositions differ from our previous models, leading to very different outcomes. The modeling details are described below.

4.1. Numerical modelling through hydrodynamical simulations

We simulate the evolution of the HeCO-WD merger with another low-mass CO-WD, by taking the latter to be an accretion torus around the former. As discussed above, the debris disks from the CO WDs were modelled following the same procedure used by us earlier (Perets et al. 2019), and discussed above, where we assume the disk composition is fully mixed, and follows the composition of the disrupted CO-WD as found in our stellar-evolution models. The HeCO WDs profiles were taken from our 1D stellar evolution modeling using MESA stellar evolution code to model the density, temperature and compositions profiles of HeCO and CO WDs as found in our previous study (Zenati et al. 2019b), which were then mapped to the 2D configuration in FLASH.

The initial conditions (see Table 1 for the properties of the different runs) were used to run our detailed hydrodynamical simulations, using the publicly available FLASH v4.3 code (Fryxell et al. 2000). In our models we employ the unsplit PPM solver of FLASH, necessary for handling artificially generated shocks, which could spread out over a few zones by the PPM hydrodynamics solver, and otherwise might lead to unphysical burning within shocks. Our simulation are in 2D axisymmetric cylindrical coordinates $[\bar{\rho}, z]$ on a grid of size $2 \times 1 [10^{10} \text{cm}]$, using an adaptive mesh refinement with a maximum of 12 levels (the finest) and a smallest grid cell of 15 km. We used a reflective boundary conditions on the symmetry axis.

We follow similar approaches as described in other works on thermonuclear SNe (e.g. Meakin et al. 2009; Perets et al. 2019) to follow the nuclear burning and detonation throughout the evolution.

We explore four different combinations of HeCO WD - CO WD mergers, in which the primary HeCO-WD disrupts the secondary; a lower mass CO-WD, forming a debris disk. Although the debris disk from the disrupted CO-WD can be initially clumpy and/or asymmetric, it rapidly evolves into a relatively symmetric accretion disk around the more massive WD before any significant nuclear burning occurs (Dan et al. 2012; Kashyap et al. 2015). We therefore model the mergers starting only following the formation of a symmetric debris disk around the more massive HeCO-WD in our simulations, similar to the approach used by us and others (Dan et al. 2015; Fernández & Metzger 2013; Zenati et al. 2019a, 2020b) to model mergers of WDs with WDs/NS. Such cylindrical symmetry of the disk and the central accreting WD allows us to model the merger in 2D. Such models are highly advantageous as they allow for high resolution simulations, with relatively little numerical expense in comparison with 3D simulation,

but they still capture most of the important multi-dimensional aspects of the merger.

Each of our hydrodynamical simulations, includes the self-gravity of the disk, and accounts for the centrifugal force as a source term. We also include neutrino heating, though it is unlikely to play an important role for the temperatures and densities reached in our models. We solve the Euler equations in axisymmetric cylindrical coordinates $[\bar{\rho}, z]$. In order not to encounter numerical issues with empty cells in the simulations, we introduce a minimal density and temperature background, which are typically taken to be $\rho_{\text{bg}} = 10^{-6} \text{g cm}^{-3}$, and $T_{\text{bg}} = 10^3 \text{K}$, and in any case, a density which is at least 100 times smaller than the density of the debris disk, and temperature which is at least 1000 times smaller.

In order to prevent the production of artificial unrealistic early detonation that may arise from insufficient numerical resolution, we applied a burning-limiter approach following (Kushnir et al. 2013). We use a detailed EOS and account for self-gravity, this is included as a potential multipole expansion of up to multipole $l_{\text{max}} = 12 - 32$ using the new FLASH multipole solver of the disk.

We use the super time-steps method in FLASH 4.0 for calculating the adaptive time-steps, which is set according to the speed-of-light Courant–Friedrichs–Lewy (CFL) condition with a CFL factor 0.2. We adopt the optimal strongly stability-preserving third-order Runge–Kutta scheme.

Using FLASH we solve the equations for mass, momentum, energy, and chemical species conservation,

$$\frac{\partial \rho}{\partial t} + \nabla \cdot (\rho \mathbf{v}) = 0, \quad (14)$$

$$\frac{d\mathbf{v}}{dt} = \mathbf{f}_c - \frac{1}{\rho} \nabla p + \nabla \phi, \quad (15)$$

$$\rho \frac{dl_z}{dt} = \bar{\rho} (\nabla \cdot \mathbf{T})_\phi \quad (16)$$

$$\rho \frac{de_{\text{int}}}{dt} + p \nabla \cdot \mathbf{v} = \frac{1}{\rho \nu} \mathbf{T} : \mathbf{T} + \rho (\dot{Q}_{\text{nuc}} - \dot{Q}_\nu), \quad (17)$$

$$\frac{\partial \mathbf{X}}{\partial t} = \dot{\mathbf{X}}, \quad (18)$$

$$\nabla^2 \phi = 4\pi G \rho + \nabla^2 \phi_c, \quad (19)$$

$$\mathbf{f}_c = \frac{l_z^2}{\bar{\rho}^3} \hat{\rho}. \quad (20)$$

These include source terms for gravity, shear viscosity, nuclear reactions, and neutrino cooling. Here, \mathbf{f}_c is an implicit centrifugal source term, where l_z is the z-component of the specific angular momentum. Variables have their standard meaning: ρ , \mathbf{v} , p , e_{int} , ν , \mathbf{T} , ϕ , and $\mathbf{X} = \{X_i\}$ denote, respectively, fluid density, poloidal velocity, total pressure, specific internal energy, fluid viscosity, viscous stress tensor for azimuthal shear, gravitational potential, and mass fractions of the isotopes X_i , with $\sum_i X_i = 1$. Furthermore, $d/dt = \partial/\partial t + \mathbf{v} \cdot \nabla$, ϕ_c denotes the HeCO-WD potential, and \dot{Q}_{nuc} and \dot{Q}_ν represent the specific nuclear heating rate

due to nuclear reactions and the specific cooling rate due to neutrino emission.

We employ the Helmholtz equation of state (EOS) free energy $F(\rho, T)$ in FLASH (Timmes & Swesty 2000b; Timmes & Arnett 1999). The Helmholtz EOS includes contributions from partially degenerate electrons and positrons, radiation, non-degenerate ions, and corrections for Coulomb effects ($P_{tot} = P_{ele} + P_{pos} + P_{ion} + P_{rad} + P_{coul}$). The most important aspect of the Helmholtz EOS is its ability to handle thermodynamic states where radiation dominates, and under conditions of very high pressure. The contributions of both nuclear reaction and neutrino cooling (Chevalier 1989; Houck & Chevalier 1991) are included in the the internal energy evolution calculations, and the Navier-Stocks equations are solved with source terms due to gravity, shear viscosity and nuclear reactions.

As discussed earlier, since our calculations are axisymmetric and do not include magnetic fields, we cannot self-consistently account for angular momentum transport due to the magneto-rotational instability or non-axisymmetric instabilities (e.g. associated with self-gravity). Instead, we make the common approximation of modeling the viscosity using the α -viscosity parameterization of Shakura & Sunyaev (1973), for which the kinematic viscosity is taken to be

$$\nu_{\alpha} = \alpha c_s^2 / \Omega_K, \quad (21)$$

where $\Omega_K = (GM_{enc}/r^3)^{1/2}$ is the Keplerian frequency given the enclosed mass M_{enc} and c_s is the sound speed. In our models we take either $\alpha = 0.1$ or $\alpha = 0.05$ (see table 1) for the dimensionless viscosity coefficient.

Nuclear burning and nucleosynthesis are followed through a 19-isotopes reaction network (Chevalier 1989). It is included in the simulations following a similar approach to that employed by us and others (e.g. Meakin et al. 2009; Zenati et al. 2019b, 2020a,b). The nuclear network used is the FLASH α -chain network of 19 isotopes, which provides the source terms \dot{X} in Eq. (18) and adequately captures the energy generated during nuclear burning \dot{Q}_{nuc} (Timmes & Swesty 2000b).

We made multiple simulations with increased resolution until convergence was reached. We found a resolution of 16 – 20km to be sufficient for convergence of up to 12% in energy.

4.2. Tracer particles and post-processing nucleosynthesis modeling

We followed the nucleosynthesis processes throughout the simulation and their key role in the evolution and the nuclear burning and explosive evolution. We made use of the 19 – isotopes reaction network in the FLASH hydrodynamical simulation, in order to follow the dynamics and the energetics of the explosive evolution. We then made use of a larger network in post-processing to follow the detailed composition of the ejecta, and allow for detailed radiative transfer modeling.

In order to do the post-processing analysis, we introduced 8000 – 20000 passive tracer particles in the various models,

to track the composition, density / entropy, and temperature of the material throughout the grid, and follow the changes in these properties, where we follow the positions and velocities of the tracer particles. The tracers were initially evenly spaced every $2 \times 10^8 cm$ throughout the WD and the debris disk.

Following the 2D FLASH runs we made use of the detailed histories of the tracer particles density and temperature to be post-processed with MESA one zone burner (Paxton et al. 2011, 2015). We employ a 125-isotope network that includes neutrons, and composite reactions from JINA’s REACLIB (Cyburt et al. 2010). Similar to our previous simulations, we find that the results from the larger network employed in the post-processing analysis showed less efficient nuclear burning, and gave rise to somewhat higher yields of intermediate elements on the expense of lower yields of iron elements, similar to the results seen in our previous models and other works (Dan et al. 2012; Perets et al. 2019).

The tracer particles and the large network post-processing were then used to generate the detailed density/composition profile of the ejecta at the end of the simulation. In turn, these data were used to produce detailed light curves and spectra of the explosions using the non-LTE CMFGEN radiative transfer code (Hillier & Dessart 2012, see more details below).

4.3. Radiative transfer modeling

The simulations with CMFGEN are 1D and are based on angular-averages of the 2D simulations performed with FLASH. When remapping these ejecta into CMFGEN, we smooth the density and elemental distribution to reduce sharp gradients. The density is smoothed by convolution with a gaussian whose standard deviation is $200 km s^{-1}$. For the abundances, we smooth by running a boxcar of width $0.01 M_{\odot}$ four times through the grid. The outer ejecta are also extended by a low density outer region with a steep density falloff in order to have an optically thin outer boundary for the radiation. The initial ejecta correspond to an epoch soon after hydrodynamical effects are over, so that the ejecta expand ballistically. At this time of a few 100 seconds, we evolve the ejecta assuming no diffusion, heating by radioactive decay, and cooling from expansion until a time of two days after explosion. At that time of two days, we remap the ejecta into CMFGEN. The radial grid typically employs 80 points.

In all simulations, radioactive decay is treated for three two-step decay chains associated with ^{56}Ni , ^{52}Fe , and ^{48}Cr (six additional decay chains were considered in (Dessart & Hillier 2015) but the corresponding isotopes are not available in the present ejecta). Decay power is treated as per normal (see, for example, Dessart et al. 2012) and proper allowance is made in the nonLTE equations for nonthermal ionization and excitation, as well as the additional heating term in the energy equation. For simplicity, we compute the non-local energy deposition by solving the radiative transfer equation with a grey absorption-only opacity to γ -rays set to $0.06 Y_e cm^2 g^{-1}$, where Y_e is the electron fraction.

The model atom used in this work includes the following atoms and ions He I (40,51), He II (13,20), C I (14,26), C II (14,26), O I (30,77), O II (30,111), Ne I (70,139), Ne II

(22,91), Na I (22,71), Mg II (22,65), Si I (100,187), Si II (31,59), Si III (33,61), S I (106,322), S II (56,324), S III (48,98), Ar I (56,110), Ar II (134,415), Ca I (76,98), Ca II (21,77), Ti II (37,152), Ti III (33,206), Cr II (28,196), Cr III (30,145), Cr IV (29,234), Mn II (25,97), Mn III (30,175), Fe I (44,136), Fe II (275,827), Fe III (83,698), Fe IV (51,294), Fe V (47,191), Co II (44,162), Co III (33,220), Co IV (37,314), Co V (32,387), Ni II (27,177), Ni III (20,107), Ni IV (36,200), and Ni V (46,183). In this list, the parentheses refer to number of super-levels and the number of full levels (see, [Hillier & Miller 1998](#) and [Hillier & Dessart 2012](#) for details).

5. RESULTS

5.1. The disk evolution and thermonuclear explosion

Our modelling begins with a debris disk assumed to have formed following the disruption of low-mass CO WD by a higher mass HeCO WD. As can be seen in Fig. 1, the disk evolves viscously, and the CO-WD debris is accreted onto the HeCO WD. The CO debris accreted onto the outer shell of the HeCO WD is then heated-up and compressed onto the He-shell of the HeCO WD, until sufficiently high temperatures and densities are reached and nuclear burning ensues. This is followed by a (weak) detonation in the He-rich material, producing nuclear burning products (see Fig. 2), and ejecting a large fraction of the burned material from the He shell of the HeCO WD and the debris disk. The explosion ejects a few times $0.1 M_{\odot}$ of mostly burned material, composed of a significant fraction of intermediate elements and in particular 20-30% in Ca; and produces $0.01-0.05 M_{\odot}$ of ^{56}Ni in the different models. We explore three pairs of WDs, and explored one of the models with a different viscosity parameter (but without using trace particles for the latter), for a total of four models, all showing a similar accretion and nuclear burning evolution, but show a range in the specific timescales of the evolution, and the overall synthesis of nuclear burning products. The model properties are listed in Table 1. The resulting ejecta, bound material and energetics are presented in Table 2. The compositions of the ejecta in the different models are summarized in Table 3.

5.2. Light curves and spectra

Using the non-LTE radiation transfer code (CMFGEN), we produce the light curves and spectra resulting from each of the models. The *UBVIRJHK* LCs are shown in Fig. 3. As can be seen in Fig. 4 and 5, the LCs compare well with the range of observed Ca-rich SNe (not including the shock breakout early peak, likely due to CSM interactions, [Jacobson-Galán et al. 2020a](#), also seen in X-rays, not modeled in the current simulations). These are also compared to various other types of SNe in Fig. 5. Fig. 8 shows the color evolution of the models in comparison with various Ia SNe and the Ca-rich SN SN 2019ehk. Fig. 6 shows the good comparison of the spectra with that of Ca-rich SNe (the detailed evolution of the modeled spectra can be seen in the appendix). Fig. 7 shows the positions of the modeled SNe in the peak-width relation in comparison with various types of SNe, showing the small differences in the WD masses can span a wide range

of behaviour, in terms of peak luminosity and the rate of LC evolution. A detailed discussion of the comparison between the modeled LCs and spectra and the observation can be found in the discussion section below.

Overall, our resulting models show excellent agreement with the observed Ca-rich SNe and their range of properties (besides the lack of clear He lines, which are observed in many of the Ca-rich SNe; this issue is discussed below). In fact, to the best of our knowledge, these are the first models to well reproduce both light curve and spectral evolution of Ca-rich SN, as well as reproduce the range of behaviors (compare with e.g. [Waldman et al. 2011](#) and [Dessart & Hillier 2015](#)). We should also note that the specific models were not chosen as to fit any of the observations, but rather we present all the models we ran to date.

5.3. Ejecta composition and line strength

As can be seen in tables 2 and 4, the resulting SNe produce large abundances of intermediate elements and low ^{56}Ni mass, consistent with the inefficient burning of He-rich material. In particular large fractions of the ejecta mass are composed of Ca, which give rise to strong Ca lines. As mentioned above, it was suggested that the Ca abundances might not need to be high in Ca-rich SN, but rather that the high nebular line ratios of Ca to O in these SNe is due to Ca being such an effective coolant, and that these objects are just O-poor ([Shen et al. 2019](#)). In our models, however, the Ca abundances are inherently very high, and our successful models are indeed Ca-rich SNe, rather than just having strong Ca lines relative to O.

We do note in regard to the OI6300 line strength could be sensitive to the relative fractions of Ca and O in different regions of the ejecta. In particular the offset in abundance between Ca and O can be very large in different regions, when the material is not well mixed (see [Dessart & Hillier 2015](#)). Since the cooling power of Ca only affects the regions where it is present, different mixing of Ca and O can potentially make large differences in the large ratios produced. In our study we made use of a 1D non-LTE code in order to model the spectra resulting from the radiative transfer analysis, and therefore needed to map the 2D simulation data into 1D, as discussed above, potentially leading to some artificial mixing and composition smoothing. We therefore should note the caveat that stronger OI6300 line might be have been produced without such artificial mixing.

6. DISCUSSION

Our models of the disruptions of low-mass CO WDs by higher mass hybrid HeCO WDs produce faint, Ca-rich SNe which agree well with the observed class of Ca-rich SNe ([Perets et al. 2010](#)), and can reproduce the range of brighter, slower-evolving Ca-rich SNe down to the fainter and faster-evolving Ca-rich SNe. In the following we discuss in detail the comparison of the models with the observations, the various possible caveats in the models and the overall implications of our results. We also briefly discuss the demographics of

Table 2. CaSNe FLASH simulation results

Model	M_{ej}^{tot}	R_{inn}	M_{bound}	M_{IME_B}	M_{IGE_B}	$M_{unbound}$	$M_{IME_{UB}}$	$M_{IGE_{UB}}$	$M_{E_{kin}}$
-	$[M_{\odot}]$	[cm]	$[M_{\odot}]$	$10^{-4}[M_{\odot}]$	$10^{-4}[M_{\odot}]$	$[M_{\odot}]$	$[M_{\odot}]$	$[M_{\odot}]$	E_{50} [erg]
fca ₁	0.457	1.5×10^8	0.081	41.24	0.858	0.377	0.167	0.022	1.693
fca ₂	0.431	1.7×10^8	0.068	30.17	0.751	0.364	0.173	0.052	1.318
fca ₃	0.365	5.2×10^8	0.075	32.16	1.127	0.288	0.159	0.012	0.951
fca ₄	0.461	1.4×10^8	0.088	40.03	0.951	0.373	0.171	0.023	1.664

Notes: The total ejecta mass calculated after five viscous timescales (Eq. 5). We show the bound/unbound ejecta calculated as positive Bernoulli parameter $\mathcal{B}e > 0$. The total unbound mass is $M_{unbound}$. The radius R_{inn} designate the position location where the weak detonation occurred in the torus mid-plane. M_{IGE_B} , $M_{IGE_{UB}}$ are the bound and unbound iron group elements where the atomic number $Z \geq 23$, respectively. M_{IME_B} , $M_{IME_{UB}}$ are the bound and unbound Intermediate elements where the atomic number $Z \geq 10$, respectively. See the 125 isotopes appendix A.

Table 3. Properties of ejecta composition for the models for which light curve and spectra were modeled using CMFGEN.

Model	C	O	Ne	Si	Ca	Ti	^{48}Cr	^{52}Fe	^{56}Ni
	$[M_{\odot}]$	$[M_{\odot}]$	$[M_{\odot}]$	$[M_{\odot}]$	$[M_{\odot}]$	$[M_{\odot}]$	$[M_{\odot}]$	$[M_{\odot}]$	$[M_{\odot}]$
fca ₁	1.01(-1)	9.91(-2)	1.24(-2)	2.32(-3)	1.40(-1)	7.97(-3)	1.01(-5)	0	2.12(-2)
fca ₂	9.38(-2)	9.09(-2)	1.17(-2)	3.34(-2)	1.09(-1)	1.48(-2)	1.97(-6)	6.86(-5)	5.00(-2)
fca ₃	8.66(-2)	1.07(-1)	5.00(-4)	8.93(-4)	1.36(-1)	7.35(-3)	3.24(-4)	5.42(-4)	1.05(-2)

Notes: Number in parentheses denote powers of ten.

Ca-rich SNe in this context, but postpone a more detailed discussion of the latter to a dedicated follow-up paper.

6.1. Comparison to Ca-rich Observations

The fca₁, fca₂ and fca₃ models contain many attributes that make them consistent with the observed properties of Ca-rich. In Figure 7 we present the Phillips relation in the B-band for a variety of SNe Ia, as well as some Ca-rich. While both the fca₁ and fca₂ models are consistent with the decline rate ($\Delta m_{15}(B)$) for Ca-rich 2007ke, PTF09dav, 2007ke, 2016hnk, and 2019ehk, the former produces a slightly fainter B-band maximum and the latter is too luminous compared to observations. Furthermore, the fca₃ model declines much faster than these Ca-rich and its maximum B-band light curve absolute magnitude is fainter, which could be consistent with some of the lowest luminosity Ca-rich events. Overall, the r–i colors (Fig. 8) of the fca₁ and fca₂ models are consistent with the observed color evolution of Ca-rich; these models also shows some consistency to the B–V colors of SNe Ia varieties shown in Figure 8 but are slightly bluer overall than SN 2019ehk’s evolution.

In Figure 4 we compare the r–band light curves of 10 Ca-rich to fca₁, fca₂ and fca₃ models. The fca₁ model provides a nearly identical match to the light curve of SN 2019ehk after the primary light curve peak, whose physical origin (e.g., circumstellar interaction or shock cooling emission) is unexplored by these models. While the evolution of the fca₂ r-band light curve matches that of observed Ca-rich, it ~ 1 -2 magnitudes brighter than most of the sample. However, the fca₂ shows a remarkable consistency with the peak magnitude and decline rate of Ca-strong SN 2016hnk, which was thought

to be either a 1991bg-like SN Ia (Galbany et al. 2019) or the result of a He-shell detonation of a sub-Chandrasekhar mass WD (Jacobson-Galán et al. 2020b). Furthermore, despite its fast rise time relative to Ca-rich, the fca₃ model matches the r-band light curve peak and decline rate of a number of objects such as iPTF16hgs, SN 2005E, PTF11kmb and SN 2021gno. The double-peaked light curve structure is not produced in either model, however, this is expected given that this phenomenon is thought to arise with shock cooling emission or shock interaction of extended circumstellar material, as observed in iPTF16hgs, SNe 2019ehk, 2021gno and 2021inl.

Additionally, fca₂ and fca₃ models appear inconsistent with observations of SNe IIb/Ib (Fig. 5; right). In terms of bolometric luminosity (Fig. 5; left), the fca₁ and fca₂ models are consistent with the evolution of SN 2019ehk during and after its secondary light curve peak, while the fca₃ model is only consistent with SN 2021gno’s peak luminosity but not its slower decline rate.

In Figure 6, we present the early- and mid-time spectra of all three models relative to observed Ca-rich SNe. Near light curve maximum, we find that the fca₁ model shows consistent spectral features of Ca II, He I and Si II to Ca-rich and even reproduces the early-time emergence of the nebular [Ca II] transition. Furthermore, the fca₁ model spectrum is very similar to SNe 2005E, 2007ke, and 2019ehk at phases ~ 20 –60 days post-maximum. At this point in their evolution, both the fca₁ model and observed Ca-rich spectra are dominated by Ca II emission as well as a weak [O I] emission profile, which is in line with the suggested observational definition of Ca-strong SNe that the line ratio [Ca II]/[O I] is greater than 2. Overall, the consistency of this explosion model indicates

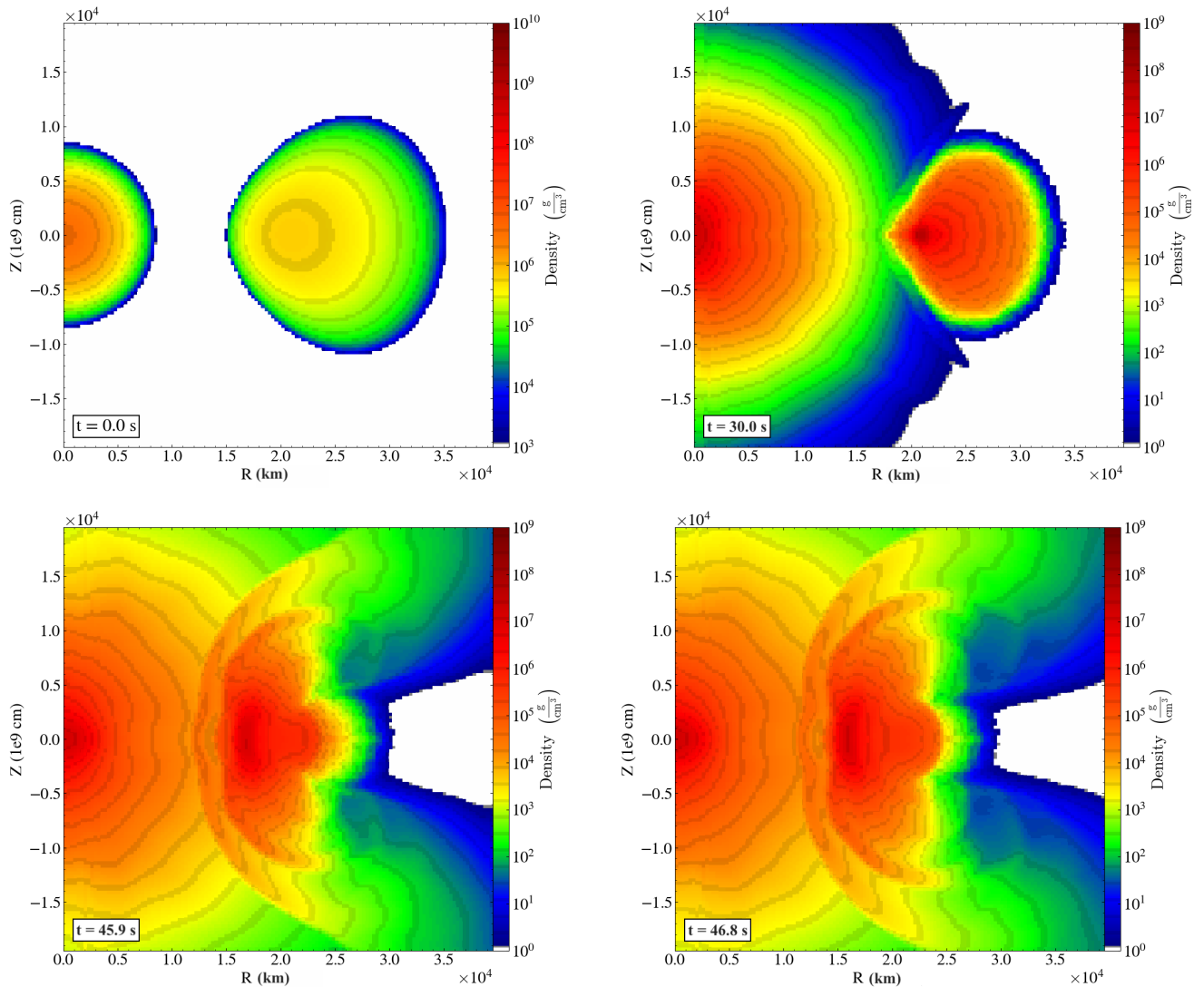


Figure 1. The evolution of the debris disk from the $0.55 M_{\odot}$ CO-WD debris disk around the HeCO-WD of mass $M = 0.63 M_{\odot}$ (see table 1; model fca₁). The panels show the color coded density distribution throughout the simulation. We show the initial model followed by several snapshots. Significant nuclear burning begins already at ~ 30 s (see also figure 2), and The detonation occurs at $t_{det} \simeq 46$ sec, which is about 88% of t_{visc}^0 .

that its ejecta structure is likely very similar to that of many observed Ca-rich.

6.2. He abundances

Our HeCO WDs are initially composed of a non-negligible He mass in the WD outer shell. However, in our current models these large He abundances existing in the initial HeCOs are mostly burned, leaving only small abundances of He in the ejecta. In particular, the He contribution is too small as to leave strong He spectral signatures. In that sense, our models can well reproduce He-poor Ca-rich SNe, but producing Ca-rich SNe with strong He line could be more challenging (though one should note that good and very secure identification of He-lines in the observed Ca-rich SNe is complex; see e.g. De et al. 2020). That being said, here we only con-

sidered a few models of HeCO WDs disrupting a CO WDs. Other branches of HeCO WDs could give rise to larger He abundances (see e.g. our discussion in Pakmor et al. 2021), and in other cases two HeCO WDs could merge (as we find in population synthesis modelling; to be discussed in a later paper). In both these cases larger He abundances are available during the disruption and explosion, potentially leaving behind much larger He abundances in the ejecta. In particular, in a preliminary model where we studied the disruption of a HeCO WD by another HeCO WD (not shown here) using similar methods, we found that the ejecta has similar IGE, has somewhat lower IME abundances, but has far larger He abundances in the ejecta ($M(\text{He}) \gtrsim 7 \times 10^{-2} M_{\odot}$ and $M(^{40}\text{Ca}) \sim 0.08 - 0.12 M_{\odot}$). This model and other more He-rich models will be discussed in a dedicated paper (Zenati,

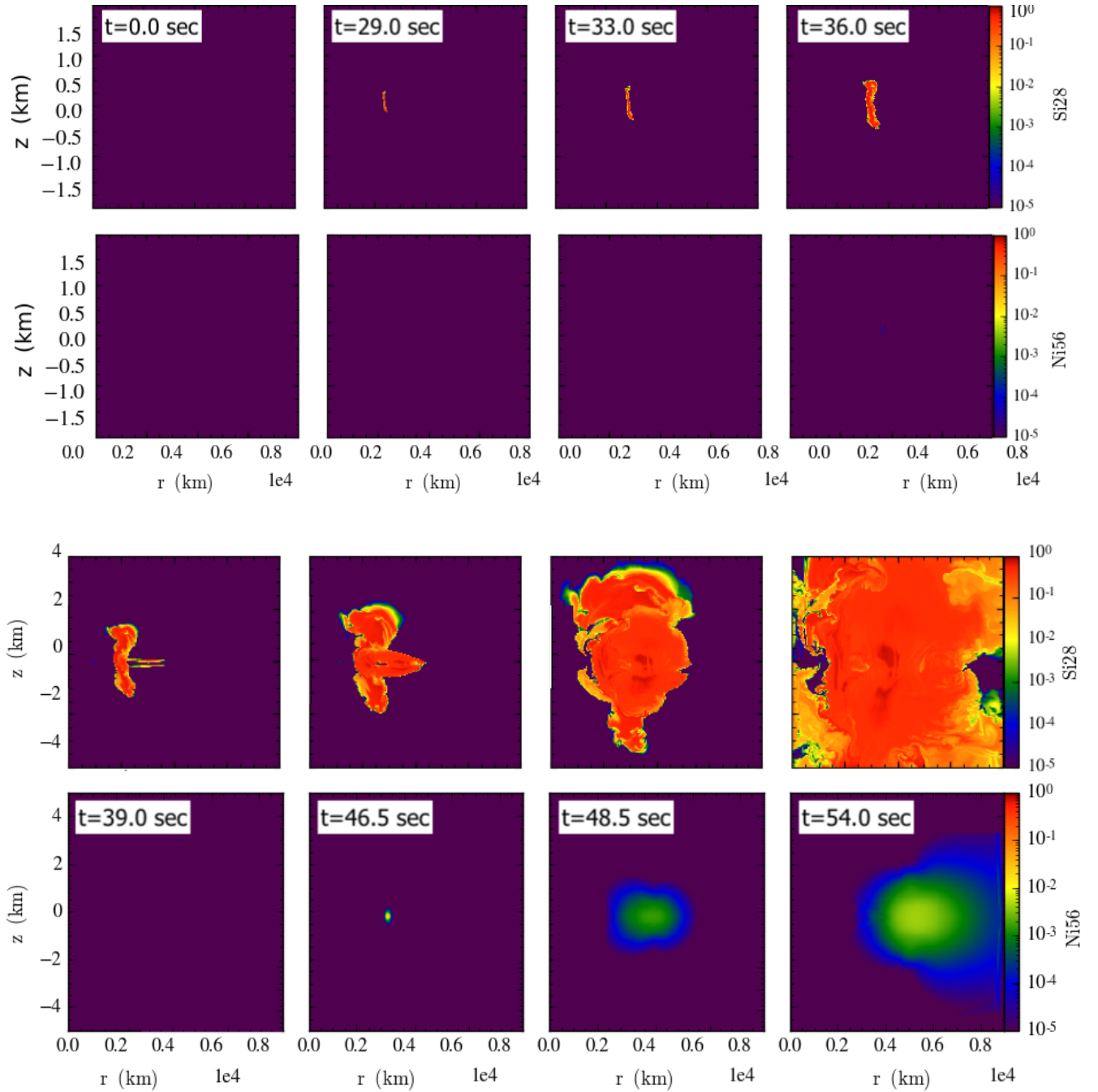


Figure 2. The evolution of model fca₁; see table 1. The two panels show the ^{28}Si and ^{56}Ni densities as a function of time. ^{28}Si production can be first seen after $t = 0.55 t_{\text{visc}}^0$ followed by ^{56}Ni production 0.4 sec after the detonation occurred. The Z-axis (upper panel) show the zoom in fluid material.

Perets et al., in prep). It is therefore possible the the He-strong Ca-rich SNe arise from a very similar channel, but in more He rich mergers due to double HeCO WDs or more He-rich HeCO WDs.

6.3. High production of Ca ^{44}Ti and the contribution of positions to the Galactic 511 keV emission

^{44}Ti is produced from the fusion of an α - nuclei with ^{40}Ca atoms. Excessive production of ^{44}Ti is therefore typically

accompanied by the excessive production of other intermediate α elements. Highly fine-tuned conditions are therefore required in order to produce large abundances of one of these isotopes without producing significant abundances of the other. Indeed, the fractional ratio of ^{44}Ti to stable Calcium, ^{40}Ca is found to be large in all studied cases of Helium-detonations. Already the original identification and characterization of Ca-rich SNe as thermonuclear SNe, inferred a large abundance of Ca, with an estimated mass of \sim

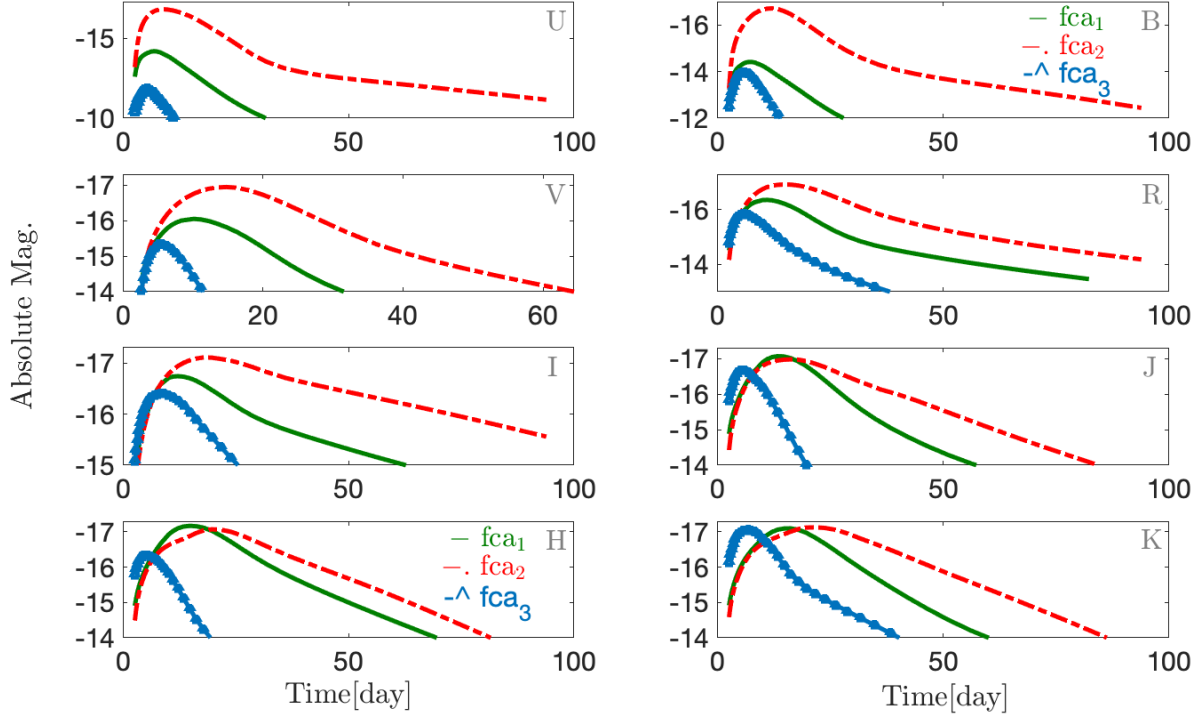


Figure 3. The light curves at different bands for the first three models in table 1.

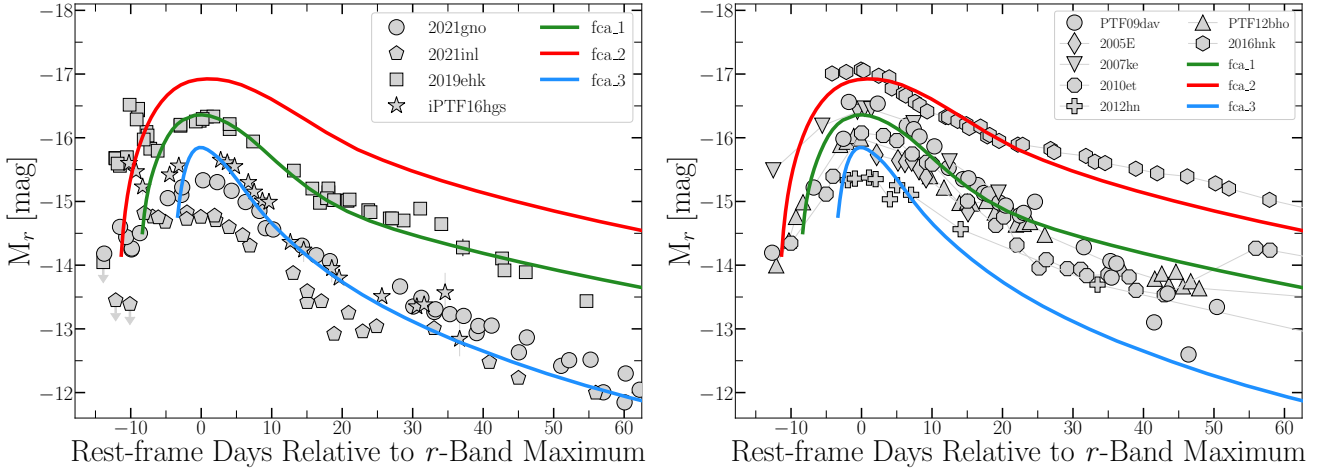


Figure 4. Left/Right: Early-time absolute r -band light curves in the AB magnitude system of fca_1 (green curve), fca_2 (blue curve) and fca_3 (red curve) with respect to other classified Ca-rich transients (Perets et al. 2010; Sullivan et al. 2011; Kasliwal et al. 2012; Lunnan et al. 2017; De et al. 2018; Jacobson-Galán et al. 2020a, 2022). Peculiar, “calcium-strong” SN2016hnk (Galbany et al. 2019; Jacobson-Galán et al. 2020b) is also presented for reference (polygons). The CaSNe fca_3 model lies between the double-peaked light curves of SN2019ehk (squares), iPTF16hgs (stars), and 2021gno (circle), as well as the light curve of PTF12bho (plus). Overall, the fca_2 model is most consistent with the light curve evolution of SN2016hnk and the fca_1 model best matches SN 2019ehk’s light curve.

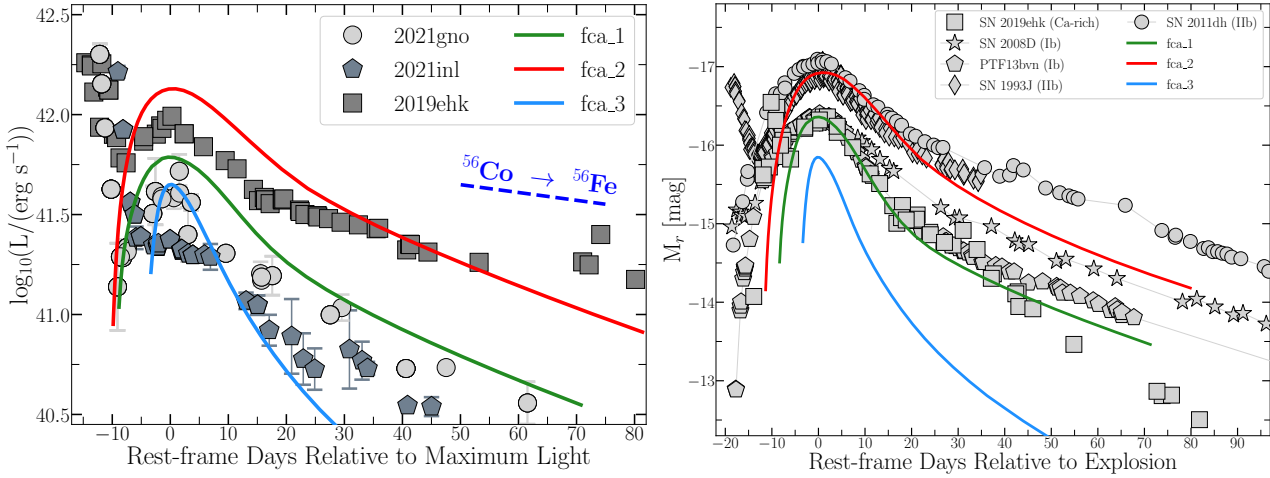


Figure 5. Left panel: The bolometric light curve of fca₁ (green curve), fca₂ (blue curve), fca₃ (red curve) compared to Ca-rich SNe 2019ehk (squares), 2021gno (circles) and 2021inl (polygons). Right panel: comparison of the three models in the r-band M_r to type Ib/Ib SNe and SN 2019ehk relative to maximum light in the AB magnitude system.

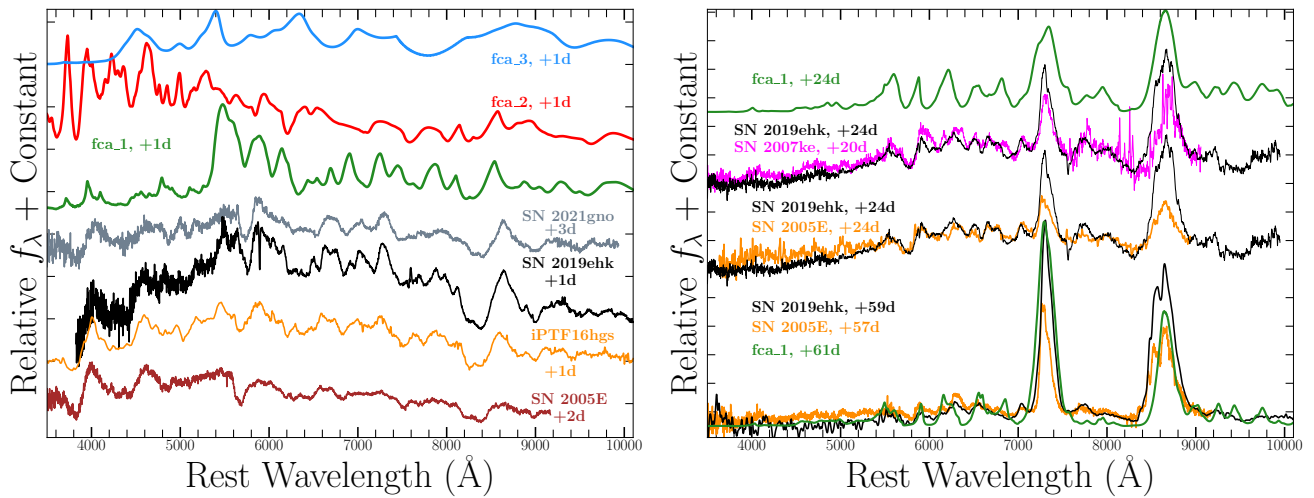


Figure 6. Left panel: Early-time spectral comparison of models fca₁ (green), fca₂ (red) and fca₃ (blue) with the observations of SN2019ehk (black) and other Ca-rich SNe at approximately the same phase. Model spectra are normalized to match the continuum of observed Ca-rich object spectra. Right panel: Direct spectral comparison of fca₁ to SN2019ehk (black) and Ca-rich SN 2007ke (magenta) and SN2005E (orange) at approximately the same phase. Model spectra are normalized to match the Ca II emission line profiles observed in SN 2019ehk. Almost every line transition is matched between spectra, with our model fca₁ showing stronger [Ca II] emission than SN 2005E.

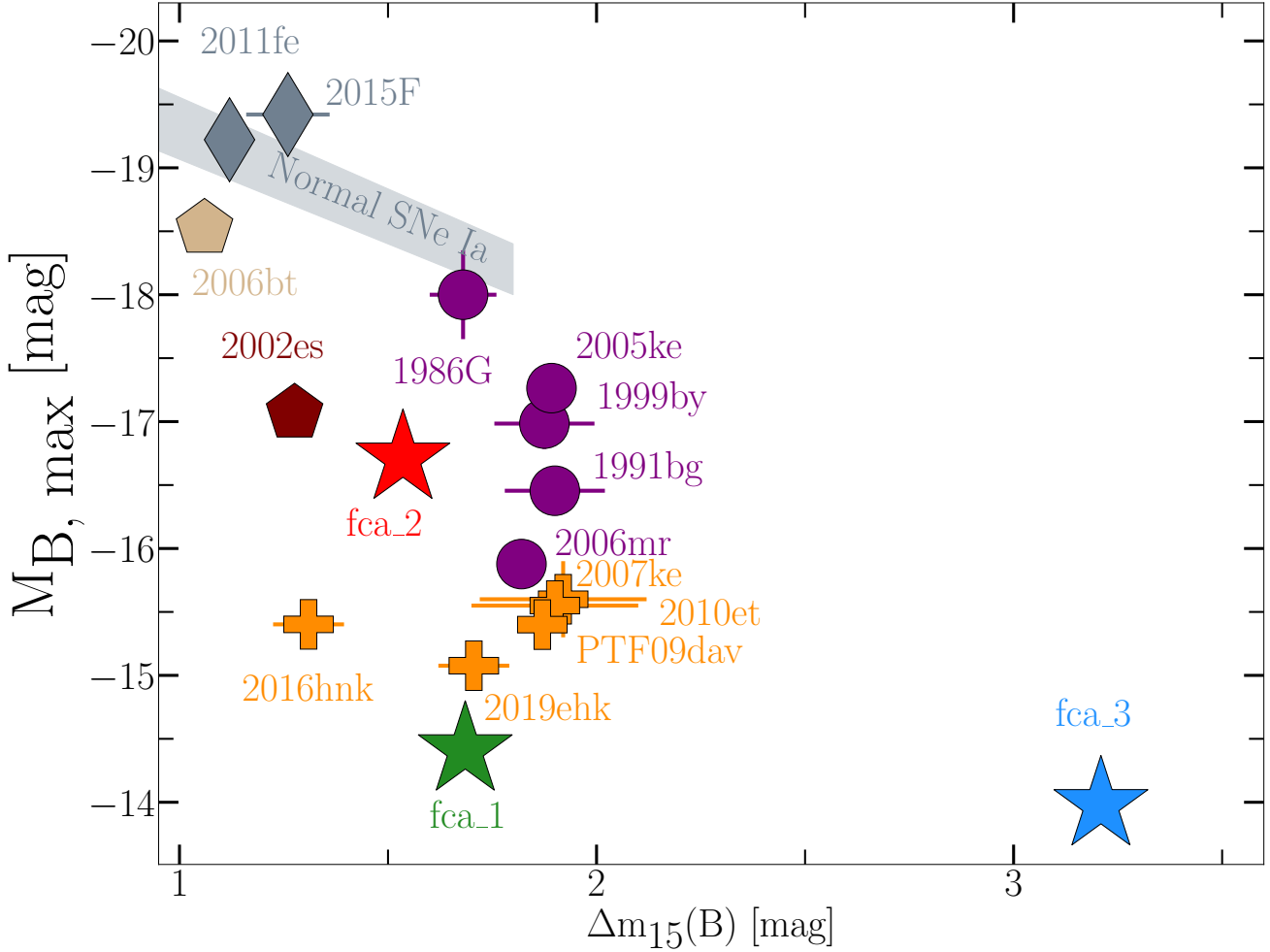


Figure 7. Illustration of Δm_{15} vs. $M_{B, \max}$ for models fca₁ (green star), fca₂ (red star) and fca₃ (blue star), and normal SNe Ia (diamonds+gray region), 91bg-like SNe Ia (circles), SNe Iax (stars), 02es-like SNe Ia (pentagons), other Ca-rich (plus signs), and peculiar thermonuclear SN 2006bt (pentagon). Some uncertainties in $M_{B, \max}$ are smaller than the plotted marker size.

0.1 M_{\odot} of Calcium in SN 2005E, the prototype SN for this type of SNe. Ca-rich SNe are therefore likely candidates as significant production sites of ^{44}Ti . By taking the range of ^{44}Ti to ^{40}Ca ratios found in theoretical models and the estimated Calcium mass in SN 2005E one can infer that large ^{44}Ti abundances should be produced.

While some of the previous models have indeed shown a large production of Ca (Waldman et al. 2011), they did not well reproduce the observed light curves. The simulations shown here do provide a potentially successful model for Ca-rich SNe. The composition of the ejecta from these models is shown in Table 4. As can be seen, Ca is indeed excessively produced in these models and as much as 20-30 % of the ejecta is composed of Ca, supporting the identification of 2005E-like SNe as Ca-rich SNe, rather than SNe with strong Ca lines, as mentioned above. Furthermore, our models show a significant production of ^{44}Ti with as much as $1.8 \times 10^{-2} M_{\odot}$ of ejected ^{44}Ti . In (Perets et al. 2010; Perets 2014) we suggested that the positrons produced through the later radioactive decay of ^{44}Ti in Ca-rich SNe could provide a

major contribution to the Galactic 511 keV emission, which origins are still not understood. Perets (2014) assumed the ^{44}Ti fractions produced in Ca-rich SNe followed the results in (Waldman et al. 2011) models, which were 1-2 orders of magnitude smaller than found in our current models. The even larger ^{44}Ti abundances found here suggest a potentially even more important contribution of Ca-rich SNe to 511 keV production, even if the rate of Ca-rich SNe in the Galactic bulge smaller than those assumed in (Perets 2014).

The large abundances of Ca initially inferred from observations (Perets et al. 2010) were suggested to play an important role in explaining the origins of enhanced Ca abundances in the intracluster medium (Perets et al. 2010; Mulchaey et al. 2014). The possibility that these SNe are only Ca strong-lined rather than inherently Ca rich (Shen et al. 2019) could potentially exclude this Ca enrichment scenario. However, our current results do support the large Ca production, and hence their potential role in explaining the composition of the intracluster medium.

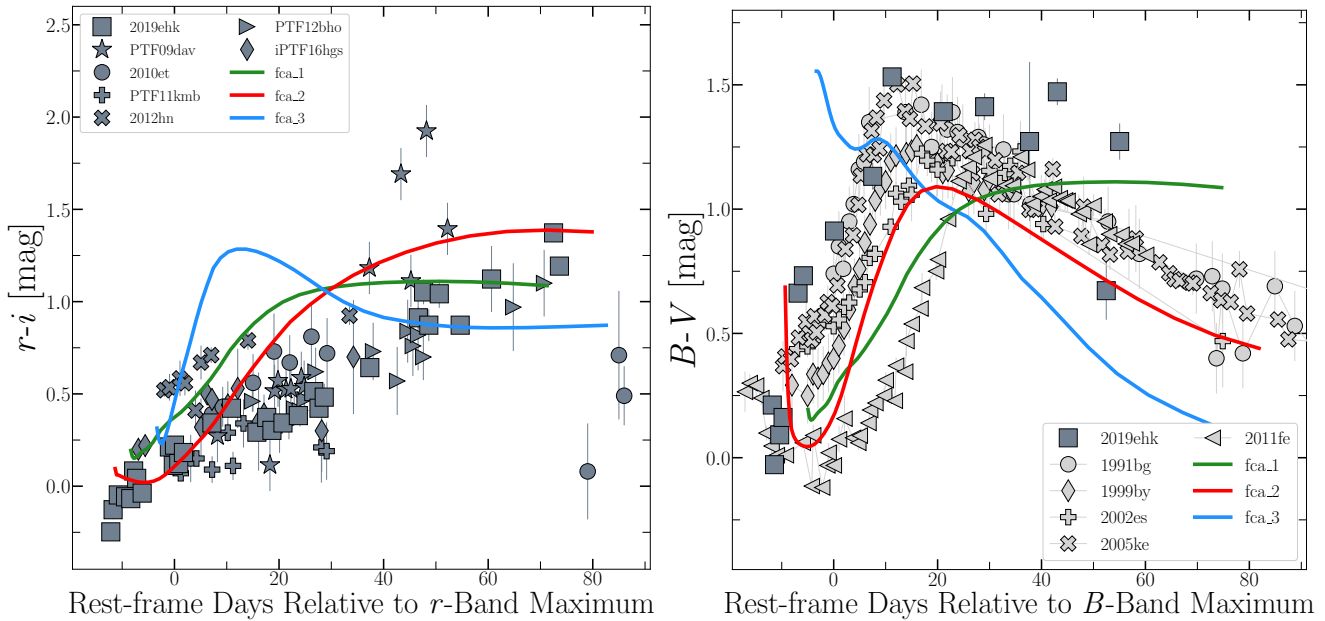


Figure 8. Color evolution comparison of models fca₁ (green curve), fca₂ (blue curve) and fca₃ (red curve) and Ca-rich. Left panel: $r-i$ color comparison of models fca₁, fca₂ and fca₃ and Ca-rich. Right Panel: $B-V$ color comparison of the three models and various types of SNe Ia and SN2019ehk.

6.4. Polarization

Our radiative transfer calculations do not model polarization, and we therefore can not directly provide any predictions in this regard. Nevertheless, we point out that our models produce non spheri-symmetric explosions, unlike our Perets et al. (2019), and others' models for normal type Ia SNe which are typically quite spherical (see, Soker 2019 table 1). Polarization measurements of type Ia SNe show them not to be polarized (or very weakly polarized) consistent with the various suggested models. We hypothesize that asphericity of our models for Ca-rich SNe would give rise to polarized radiation. Polarization measurement are typically quite difficult and require significant fluxes, but future polarization measurements of sufficiently close-by Ca-rich SNe might be possible, and could test this prediction, and, if correct, show them to be far more polarized than normal type Ia SNe.

6.5. Possible caveats

While potentially providing the first successful model for Ca-rich SNe, one needs to consider several potential caveats.

- Our models are axisymmetric 2D models, and in particular do not consider the early disruption stage. Our disk models are therefore not directly derived from a self-consistent modeling of the disk formation, which might differ from the hypothesised disk used in our models.
- Our radiative transfer modeling is 1D, while the explosion is likely not spheri-symmetric, and a 2D, or better 3D radiative transfer modeling might be required in order to better represent the predicted light-curve and spectra.

- The viscous evolution of our disks is modeled simplistically through artificial Shakura-Sunayev viscosity, and a more realistic evolution could potentially affect the results.
- While our models provide good match for Ca-rich SNe, they poorly He-lines compare to the observed for many of the Ca-rich SNe, suggesting more He should exist in the ejecta (though as we briefly discuss this issue might be alleviated with HeCO-HeCO WD mergers of more He-enriched HeCO WDs).

Future 3D modeling of mergers (currently in progress) and 3D radiative transfer models might resolve the first two issues, and extending our models to double HeCO WDs (in progress) and more He-enriched HeCO WDs would allow us to test the possibility of producing more He-rich Ca-rich SNe.

In regards to the viscosity, we have run one of the models with a different viscosity parameter, as to get a handle of its influence (see Table 1). The resulting evolution, explosion energetics and composition, while somewhat quantitatively different than the original model, do show a similar qualitative behaviour, providing support to the robustness of the results in this regard. Nevertheless, more realistic simulations of this issue could better test this.

7. Ca-rich SNE DEMOGRAPHICS AND ENVIRONMENTS

Ca-rich SNe are observed both in early type and late type galaxies, but they are far more abundant in early type galaxies compared with normal type Ia SNe (e.g. Perets et al. 2010; Kasliwal et al. 2012; Lyman et al. 2013; De et al. 2020), and typically explode far from star-forming regions, suggesting a

#	fca1 _{unbound} [M _⊙]	fca2 _{unbound} [M _⊙]	fca3 _{unbound} [M _⊙]	fca1 _{bound} [M _⊙]	fca2 _{bound} [M _⊙]	fca3 _{bound} [M _⊙]
¹ H	1.31×10^{-5}	4.18×10^{-5}	6.05×10^{-5}	2.77×10^{-5}	1.69×10^{-5}	2.38×10^{-5}
⁴ He	2.55×10^{-3}	9.27×10^{-4}	8.35×10^{-4}	8.47×10^{-3}	4.83×10^{-3}	3.77×10^{-3}
¹² C	1.01×10^{-1}	1.04×10^{-1}	8.84×10^{-2}	4.86×10^{-2}	5.39×10^{-2}	5.62×10^{-2}
¹⁴ N	1.69×10^{-7}	3.62×10^{-7}	1.68×10^{-6}	3.46×10^{-7}	1.45×10^{-7}	5.32×10^{-7}
¹⁶ O	9.82×10^{-2}	9.91×10^{-1}	1.55×10^{-1}	4.56×10^{-2}	2.97×10^{-2}	4.22×10^{-2}
²⁰ Ne	8.24×10^{-3}	1.12×10^{-2}	1.19×10^{-2}	3.28×10^{-5}	3.42×10^{-4}	8.48×10^{-5}
²⁴ Mg	3.17×10^{-3}	1.83×10^{-5}	5.08×10^{-5}	7.63×10^{-5}	6.33×10^{-6}	3.26×10^{-6}
²⁸ Si	2.28×10^{-3}	3.31×10^{-2}	8.89×10^{-4}	1.31×10^{-3}	1.07×10^{-3}	2.08×10^{-3}
³² S	8.23×10^{-3}	6.44×10^{-3}	2.65×10^{-3}	2.46×10^{-4}	2.61×10^{-4}	1.12×10^{-4}
³⁵ Cl	3.19×10^{-4}	3.05×10^{-4}	8.51×10^{-4}	1.62×10^{-5}	2.51×10^{-5}	1.96×10^{-5}
³⁶ Ar	6.57×10^{-4}	7.92×10^{-4}	1.99×10^{-4}	7.32×10^{-4}	1.42×10^{-4}	2.15×10^{-5}
⁴⁰ Ca	1.37×10^{-1}	1.08×10^{-1}	1.34×10^{-1}	3.06×10^{-3}	1.58×10^{-3}	8.16×10^{-4}
⁴⁴ Ti	7.94×10^{-3}	1.46×10^{-2}	7.34×10^{-3}	2.41×10^{-4}	6.03×10^{-4}	2.15×10^{-4}
⁴⁸ Cr	1.02×10^{-5}	1.94×10^{-6}	3.24×10^{-4}	4.02×10^{-6}	1.06×10^{-6}	4.52×10^{-6}
⁵² Fe	2.44×10^{-5}	7.03×10^{-5}	5.51×10^{-4}	1.16×10^{-7}	2.82×10^{-6}	4.35×10^{-5}
⁵⁴ Fe	5.29×10^{-4}	1.19×10^{-3}	1.54×10^{-3}	1.66×10^{-5}	4.59×10^{-6}	2.13×10^{-5}
⁵⁶ Ni	2.12×10^{-2}	5.05×10^{-2}	1.06×10^{-2}	5.33×10^{-5}	7.12×10^{-5}	6.02×10^{-5}

Table 4. The unbound and bound material of the ejecta mass of all models.

much older progenitor population for these SNe (Perets et al. 2010, 2011a; Lyman et al. 2013). Such SNe are also observed in relatively large offsets from their host galaxy nuclei when observed in early type galaxies (Perets et al. 2010; Perets 2014; Foley 2015; Perets & Beniamini 2021), consistent with the existence of large old stellar populations at the large halos of early type galaxies (Perets & Beniamini 2021). Together, these suggest an overall a delay time distribution far more skewed towards long Gyrs delays compared with normal type Ia SNe. Assuming hybrid HeCO WDs disrupting lower-mass WDs are the progenitors of Ca-rich SNe, as suggested here, one can explore the rates of such SNe and their delay time distribution using population synthesis studies. The data in our original population synthesis study in (Perets et al. 2019) included information on such progenitors; analyzing these data we found the such progenitors can produce rates as large as a few up to 15% of the normal type Ia rate, and can have very long delays, far more extended than normal type Ia SNe. These are potentially consistent with the observed rates and demographics of Ca-rich SNe. However, these could be sensitive to the exact choice of the mass limits of the HeCO and CO WD progenitors, the metallicities etc. We therefore postpone the detailed exploration of these issues to a dedicated paper (Toonen et al., in prep.).

8. SUMMARY

When we first characterized Ca-rich SNe as belonging to a unique novel type of faint, Ca and He-rich SNe, we found many of them explode in very old environments (Perets et al. 2010), and inferred them to have low mass ejecta. These findings already excluded a core-collapse origin for at the

majority of these SNe, and pointed to a likely thermonuclear origin, arising from a He-rich explosion of a WD. Extensive observational studies of these SNe over the last decade far improved and extended our understanding of their properties. It showed them to be more diverse than originally thought (Kasliwal et al. 2012; De et al. 2020), and include He-poor (type Ia/c) SNe, and the existence of early CSM interactions (Jacobson-Galán et al. 2020a). Less progress was done on the theoretical understanding of these SNe.

Decades ago (Woosley et al. 1986) found that that detonation of large He-shells on low-mass WDs (suggested to form following long-term mass-transfer onto a WD from a stellar companion) might produce ⁵⁶Ni poor, and possibly Ca-rich SNe. These were not likely to resemble normal type Ia SNe, and, consequently, they attracted little interest and follow-up studies at the time (although they were suggested to be related to rapidly evolving SNe 1885A and 1939B; de Vaucouleurs & Corwin 1985; Perets et al. 2011b).

The finding and characterization of a novel type of faint, Ca-rich SNe (Perets et al. 2010) renewed the interest in such He-shell detonation models, together with more modern incarnations of the (Woosley et al. 1986), termed .Ia SNe (Bildsten et al. 2007) which considered large He-shell detonation models. These models, and new ones that produced for the first time detailed light curve and spectra of such scenarios, while having some success in producing the observed and/or inferred properties of Ca-rich SNe, did not well reproduce the overall properties (Waldman et al. 2011; Dessart & Hillier 2015). Suggestions of NS mergers with WDs were also explored as possible progenitors (Fernández & Metzger 2013), but more detailed studies of such explosions excluded these

as potential progenitors for Ca-rich SNe (Zenati et al. 2019a; Toonen et al. 2018).

Here we proposed a novel model for the origin of Ca-rich SNe from the disruption of low-mass CO WDs by hybrid HeCO WDs, and the subsequent accretion of the CO-WD debris on the HeCO WD. We made use of 2D hydrodynamical-thermonuclear simulations of the evolution of the debris disk, and showed a weak He-rich detonation ensues following the accretion of CO material on the HeCO He-shell (surface). This weak explosion ejects a few $0.1 M_{\odot}$ of intermediate-elements rich material and produce up to a few $0.01 M_{\odot}$ of ^{56}Ni . Using nucleosynthesis post-processing and non-LTE radiation transport simulations, we modeled the light-curve and spectra of such explosions, and showed them to well match the light curve and spectra of Ca-rich SNe.

We modeled three different HeCO-WD CO-WD pairs, which produce a range of Ca-rich explosive transients, providing the best models to date for the light curves and spectra

of Ca-rich SNe, and potentially explaining the range of observed Ca-rich SNe (those not showing clear He lines). We suggest that the models of double HeCO WD mergers and/or more enriched HeCO WDs might also produce Ca-rich SNe with more pronounced He lines.

ACKNOWLEDGEMENTS

YZ thanks Kevin Schlaufman and Colin Norman for helpful discussions. YZ and HBP acknowledge support for this project from the European Union's Horizon 2020 research and innovation program under grant agreement No 865932-ERC-SNeX. W.J-G is supported by the National Science Foundation Graduate Research Fellowship Program under Grant No. DGE-1842165. W.J-G acknowledges support through NASA grants in support of *Hubble Space Telescope* programs GO-16075 and 16500. FLASH simulations were performed on the Astric computer cluster of the Israeli I-CORE center. The plots in this paper have been generated using Matplotlib (Hunter 2007) and yt-project (Turk et al. 2011).

REFERENCES

- Balbus, S. A., & Hawley, J. F. 1998, *Reviews of Modern Physics*, 70, 1, doi: [10.1103/RevModPhys.70.1](https://doi.org/10.1103/RevModPhys.70.1)
- Bildsten, L., Shen, K. J., Weinberg, N. N., & Nelemans, G. 2007, *ApJL*, 662, L95, doi: [10.1086/519489](https://doi.org/10.1086/519489)
- Bobrick, A., Davies, M. B., & Church, R. P. 2017, *MNRAS*, 467, 3556, doi: [10.1093/mnras/stx312](https://doi.org/10.1093/mnras/stx312)
- Bobrick, A., Zenati, Y., Perets, H. B., Davies, M. B., & Church, R. 2021, arXiv e-prints, arXiv:2104.03415. <https://arxiv.org/abs/2104.03415>
- Chen, H.-L., Tauris, T. M., Chen, X., & Han, Z. 2022, *ApJ*, 930, 134, doi: [10.3847/1538-4357/ac6608](https://doi.org/10.3847/1538-4357/ac6608)
- Chevalier, R. A. 1989, *ApJ*, 346, 847, doi: [10.1086/168066](https://doi.org/10.1086/168066)
- Cyburt, R. H., Amthor, A. M., Ferguson, R., et al. 2010, *ApJS*, 189, 240, doi: [10.1088/0067-0049/189/1/240](https://doi.org/10.1088/0067-0049/189/1/240)
- Dan, M., Guillochon, J., Brügggen, M., Ramirez-Ruiz, E., & Rosswog, S. 2015, *MNRAS*, 454, 4411, doi: [10.1093/mnras/stv2289](https://doi.org/10.1093/mnras/stv2289)
- Dan, M., Rosswog, S., Guillochon, J., & Ramirez-Ruiz, E. 2012, *MNRAS*, 422, 2417, doi: [10.1111/j.1365-2966.2012.20794.x](https://doi.org/10.1111/j.1365-2966.2012.20794.x)
- De, K., Fremling, U. C., Gal-Yam, A., et al. 2021, *ApJL*, 907, L18, doi: [10.3847/2041-8213/abd627](https://doi.org/10.3847/2041-8213/abd627)
- De, K., Kasliwal, M. M., Cantwell, T., et al. 2018, *ApJ*, 866, 72, doi: [10.3847/1538-4357/aadf8e](https://doi.org/10.3847/1538-4357/aadf8e)
- De, K., Kasliwal, M. M., Tzanidakis, A., et al. 2020, arXiv e-prints, arXiv:2004.09029. <https://arxiv.org/abs/2004.09029>
- de Vaucouleurs, G., & Corwin, H. G., J. 1985, *ApJ*, 295, 287, doi: [10.1086/163374](https://doi.org/10.1086/163374)
- Dessart, L., & Hillier, D. J. 2015, *MNRAS*, 447, 1370, doi: [10.1093/mnras/stu2520](https://doi.org/10.1093/mnras/stu2520)
- Dessart, L., Hillier, D. J., Li, C., & Woosley, S. 2012, *MNRAS*, 424, 2139, doi: [10.1111/j.1365-2966.2012.21374.x](https://doi.org/10.1111/j.1365-2966.2012.21374.x)
- Eggleton, P. P. 1983, *ApJ*, 268, 368, doi: [10.1086/160960](https://doi.org/10.1086/160960)
- Fernández, R., & Metzger, B. D. 2013, *ApJ*, 763, 108, doi: [10.1088/0004-637X/763/2/108](https://doi.org/10.1088/0004-637X/763/2/108)
- Foley, R. J. 2015, *MNRAS*, 452, 2463, doi: [10.1093/mnras/stv789](https://doi.org/10.1093/mnras/stv789)
- Fryer, C. L., Woosley, S. E., Herant, M., & Davies, M. B. 1999, *ApJ*, 520, 650, doi: [10.1086/307467](https://doi.org/10.1086/307467)
- Fryxell, B., Olson, K., Ricker, P., et al. 2000, *ApJS*, 131, 273, doi: [10.1086/317361](https://doi.org/10.1086/317361)
- Galbany, L., Ashall, C., Hoefflich, P., et al. 2019, arXiv e-prints, arXiv:1904.10034. <https://arxiv.org/abs/1904.10034>
- Han, Z., Podsiadlowski, P., & Lynas-Gray, A. E. 2007, *MNRAS*, 380, 1098, doi: [10.1111/j.1365-2966.2007.12151.x](https://doi.org/10.1111/j.1365-2966.2007.12151.x)
- Hillier, D. J., & Dessart, L. 2012, *MNRAS*, 424, 252, doi: [10.1111/j.1365-2966.2012.21192.x](https://doi.org/10.1111/j.1365-2966.2012.21192.x)
- Hillier, D. J., & Miller, D. L. 1998, *ApJ*, 496, 407, doi: [10.1086/305350](https://doi.org/10.1086/305350)
- Houck, J. C., & Chevalier, R. A. 1991, *ApJ*, 376, 234, doi: [10.1086/170272](https://doi.org/10.1086/170272)
- Hunter, J. D. 2007, *Computing in Science & Engineering*, 9, 90, doi: [10.1109/MCSE.2007.55](https://doi.org/10.1109/MCSE.2007.55)
- Iben, I., J., & Tutukov, A. V. 1985, *ApJS*, 58, 661, doi: [10.1086/191054](https://doi.org/10.1086/191054)
- Jacobson-Galán, W., Venkatraman, P., Margutti, R., et al. 2022, arXiv e-prints, arXiv:2203.03785. <https://arxiv.org/abs/2203.03785>
- Jacobson-Galán, W. V., Margutti, R., Kilpatrick, C. D., et al. 2020a, *ApJ*, 898, 166, doi: [10.3847/1538-4357/ab9e66](https://doi.org/10.3847/1538-4357/ab9e66)

- Jacobson-Galán, W. V., Polin, A., Foley, R. J., et al. 2020b, *ApJ*, 896, 165, doi: [10.3847/1538-4357/ab94b8](https://doi.org/10.3847/1538-4357/ab94b8)
- Jacobson-Galán, W. V., Margutti, R., Kilpatrick, C. D., et al. 2021, *ApJL*, 908, L32, doi: [10.3847/2041-8213/abdebc](https://doi.org/10.3847/2041-8213/abdebc)
- Kashyap, R., Fisher, R., García-Berro, E., et al. 2015, *ApJL*, 800, L7, doi: [10.1088/2041-8205/800/1/L7](https://doi.org/10.1088/2041-8205/800/1/L7)
- Kasliwal, M. M., Kulkarni, S. R., Gal-Yam, A., et al. 2010, *ApJ*, 723, L98, doi: [10.1088/2041-8205/723/1/L98](https://doi.org/10.1088/2041-8205/723/1/L98)
- . 2012, *ApJ*, 755, 161, doi: [10.1088/0004-637X/755/2/161](https://doi.org/10.1088/0004-637X/755/2/161)
- Kushnir, D., Katz, B., Dong, S., Livne, E., & Fernández, R. 2013, *ApJL*, 778, L37, doi: [10.1088/2041-8205/778/2/L37](https://doi.org/10.1088/2041-8205/778/2/L37)
- Lunnan, R., Kasliwal, M. M., Cao, Y., et al. 2017, *ApJ*, 836, 60, doi: [10.3847/1538-4357/836/1/60](https://doi.org/10.3847/1538-4357/836/1/60)
- Lyman, J. D., James, P. A., Perets, H. B., et al. 2013, *MNRAS*, 434, 527, doi: [10.1093/mnras/stt1038](https://doi.org/10.1093/mnras/stt1038)
- MacLeod, M., Goldstein, J., Ramirez-Ruiz, E., Guillochon, J., & Samsing, J. 2014, *ApJ*, 794, 9, doi: [10.1088/0004-637X/794/1/9](https://doi.org/10.1088/0004-637X/794/1/9)
- Maoz, D., Hallakoun, N., & Badenes, C. 2018, *MNRAS*, 476, 2584, doi: [10.1093/mnras/sty339](https://doi.org/10.1093/mnras/sty339)
- Margalit, B., & Metzger, B. D. 2016, *MNRAS*, 461, 1154, doi: [10.1093/mnras/stw1410](https://doi.org/10.1093/mnras/stw1410)
- Meakin, C. A., Seitzzahl, I., Townsley, D., et al. 2009, *ApJ*, 693, 1188, doi: [10.1088/0004-637X/693/2/1188](https://doi.org/10.1088/0004-637X/693/2/1188)
- Metzger, B. D. 2012, *MNRAS*, 419, 827, doi: [10.1111/j.1365-2966.2011.19747.x](https://doi.org/10.1111/j.1365-2966.2011.19747.x)
- Metzger, B. D., Zenati, Y., Chomiuk, L., Shen, K. J., & Strader, J. 2021, *ApJ*, 923, 100, doi: [10.3847/1538-4357/ac2a39](https://doi.org/10.3847/1538-4357/ac2a39)
- Mulchaey, J. S., Kasliwal, M. M., & Kollmeier, J. A. 2014, *ApJL*, 780, L34, doi: [10.1088/2041-8205/780/2/L34](https://doi.org/10.1088/2041-8205/780/2/L34)
- Nakaoka, T., Maeda, K., Yamanaka, M., et al. 2021, *ApJ*, 912, 30, doi: [10.3847/1538-4357/abe765](https://doi.org/10.3847/1538-4357/abe765)
- Nelson, L. A., Rappaport, S. A., & Joss, P. C. 1986, *ApJ*, 304, 231, doi: [10.1086/164156](https://doi.org/10.1086/164156)
- Pakmor, R., Zenati, Y., Perets, H. B., & Toonen, S. 2021, *MNRAS*, 503, 4734, doi: [10.1093/mnras/stab686](https://doi.org/10.1093/mnras/stab686)
- Papaloizou, J. C. B., & Pringle, J. E. 1984, *MNRAS*, 208, 721, doi: [10.1093/mnras/208.4.721](https://doi.org/10.1093/mnras/208.4.721)
- Paxton, B., Bildsten, L., Dotter, A., et al. 2011, *ApJS*, 192, 3, doi: [10.1088/0067-0049/192/1/3](https://doi.org/10.1088/0067-0049/192/1/3)
- Paxton, B., Marchant, P., Schwab, J., et al. 2015, *ApJS*, 220, 15, doi: [10.1088/0067-0049/220/1/15](https://doi.org/10.1088/0067-0049/220/1/15)
- Perets, H. B. 2014, arXiv e-prints, arXiv:1407.2254. <https://arxiv.org/abs/1407.2254>
- Perets, H. B., Badenes, C., Arcavi, I., Simon, J. D., & Gal-yam, A. 2011a, *ApJ*, 730, 89, doi: [10.1088/0004-637X/730/2/89](https://doi.org/10.1088/0004-637X/730/2/89)
- . 2011b, *ApJ*, 730, 89, doi: [10.1088/0004-637X/730/2/89](https://doi.org/10.1088/0004-637X/730/2/89)
- Perets, H. B., & Beniamini, P. 2021, *MNRAS*, 503, 5997, doi: [10.1093/mnras/stab794](https://doi.org/10.1093/mnras/stab794)
- Perets, H. B., Zenati, Y., Toonen, S., & Bobrick, A. 2019, arXiv e-prints, arXiv:1910.07532. <https://arxiv.org/abs/1910.07532>
- Perets, H. B., Gal-Yam, A., Mazzali, P. A., et al. 2010, *Nature*, 465, 322, doi: [10.1038/nature09056](https://doi.org/10.1038/nature09056)
- Prada Moroni, P. G., & Straniero, O. 2009, *A&A*, 507, 1575, doi: [10.1051/0004-6361/200912847](https://doi.org/10.1051/0004-6361/200912847)
- Shakura, N. I., & Sunyaev, R. A. 1973, *A&A*, 24, 337
- Shen, K. J., Kasen, D., Weinberg, N. N., Bildsten, L., & Scannapieco, E. 2010, *ApJ*, 715, 767, doi: [10.1088/0004-637X/715/2/767](https://doi.org/10.1088/0004-637X/715/2/767)
- Shen, K. J., Quataert, E., & Pakmor, R. 2019, *ApJ*, 887, 180, doi: [10.3847/1538-4357/ab5370](https://doi.org/10.3847/1538-4357/ab5370)
- Soker, N. 2019, *NewAR*, 87, 101535, doi: [10.1016/j.newar.2020.101535](https://doi.org/10.1016/j.newar.2020.101535)
- Stone, J. M., Pringle, J. E., & Begelman, M. C. 1999, *MNRAS*, 310, 1002, doi: [10.1046/j.1365-8711.1999.03024.x](https://doi.org/10.1046/j.1365-8711.1999.03024.x)
- Sullivan, M., Kasliwal, M. M., Nugent, P. E., et al. 2011, *ApJ*, 732, 118, doi: [10.1088/0004-637X/732/2/118](https://doi.org/10.1088/0004-637X/732/2/118)
- Timmes, F. X., & Arnett, D. 1999, *ApJS*, 125, 277, doi: [10.1086/313271](https://doi.org/10.1086/313271)
- Timmes, F. X., & Swesty, F. D. 2000a, *ApJS*, 126, 501, doi: [10.1086/313304](https://doi.org/10.1086/313304)
- . 2000b, *ApJS*, 126, 501, doi: [10.1086/313304](https://doi.org/10.1086/313304)
- Toomre, A. 1964, *ApJ*, 139, 1217, doi: [10.1086/147861](https://doi.org/10.1086/147861)
- Toonen, S., Perets, H. B., Igoshev, A. P., Michaely, E., & Zenati, Y. 2018, *A&A*, 619, A53, doi: [10.1051/0004-6361/201833164](https://doi.org/10.1051/0004-6361/201833164)
- Turk, M. J., Smith, B. D., Oishi, J. S., et al. 2011, *ApJS*, 192, 9, doi: [10.1088/0067-0049/192/1/9](https://doi.org/10.1088/0067-0049/192/1/9)
- Waldman, R., Sauer, D., Livne, E., et al. 2011, *ApJ*, 738, 21, doi: [10.1088/0004-637X/738/1/21](https://doi.org/10.1088/0004-637X/738/1/21)
- Woolley, S. E., Taam, R. E., & Weaver, T. A. 1986, *ApJ*, 301, 601, doi: [10.1086/163926](https://doi.org/10.1086/163926)
- Zenati, Y., Bobrick, A., & Perets, H. B. 2020a, *MNRAS*, 493, 3956, doi: [10.1093/mnras/staa507](https://doi.org/10.1093/mnras/staa507)
- Zenati, Y., Perets, H. B., & Toonen, S. 2019a, *MNRAS*, 486, 1805, doi: [10.1093/mnras/stz316](https://doi.org/10.1093/mnras/stz316)
- Zenati, Y., Siegel, D. M., Metzger, B. D., & Perets, H. B. 2020b, *MNRAS*, 499, 4097, doi: [10.1093/mnras/staa3002](https://doi.org/10.1093/mnras/staa3002)
- Zenati, Y., Toonen, S., & Perets, H. B. 2019b, *MNRAS*, 482, 1135, doi: [10.1093/mnras/sty2723](https://doi.org/10.1093/mnras/sty2723)

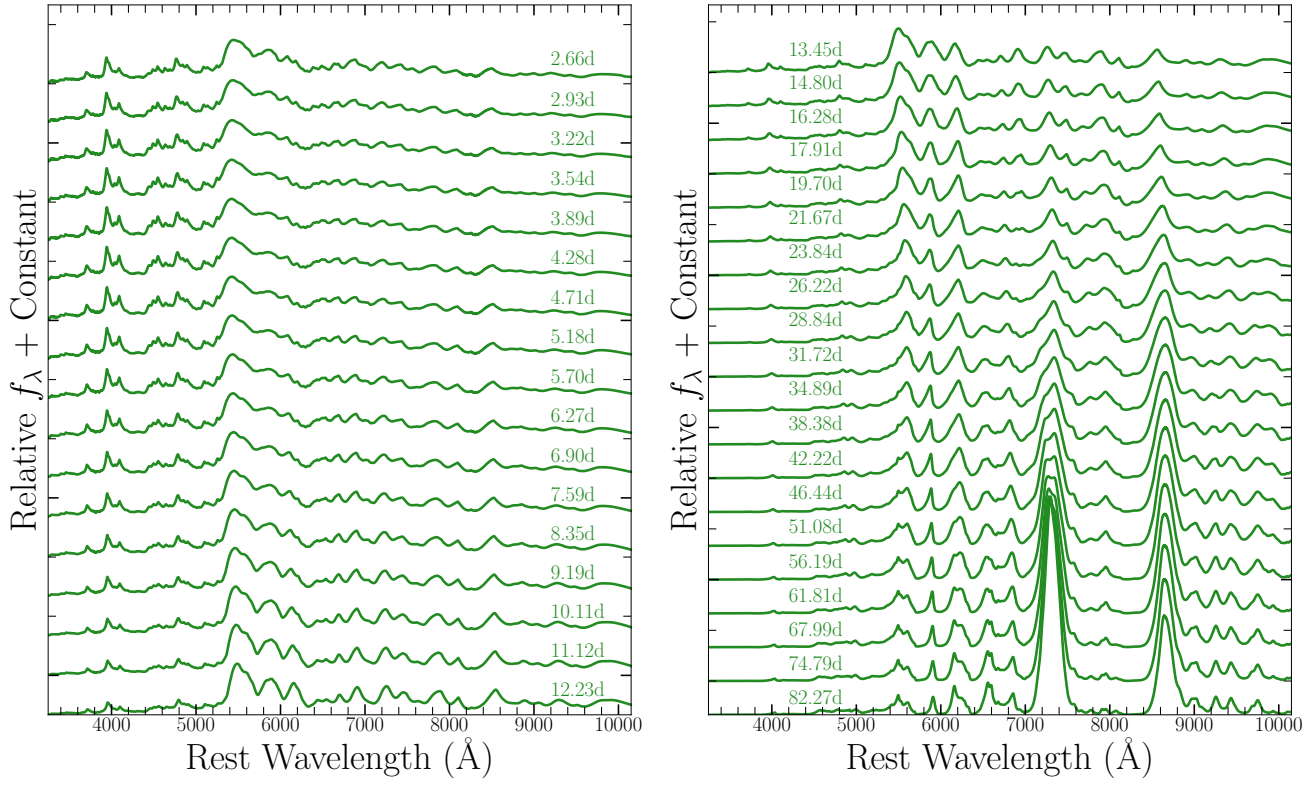


Figure 9. Spectral series of fca_1 model. Each spectrum is normalized by the mean spectral flux.

APPENDIX

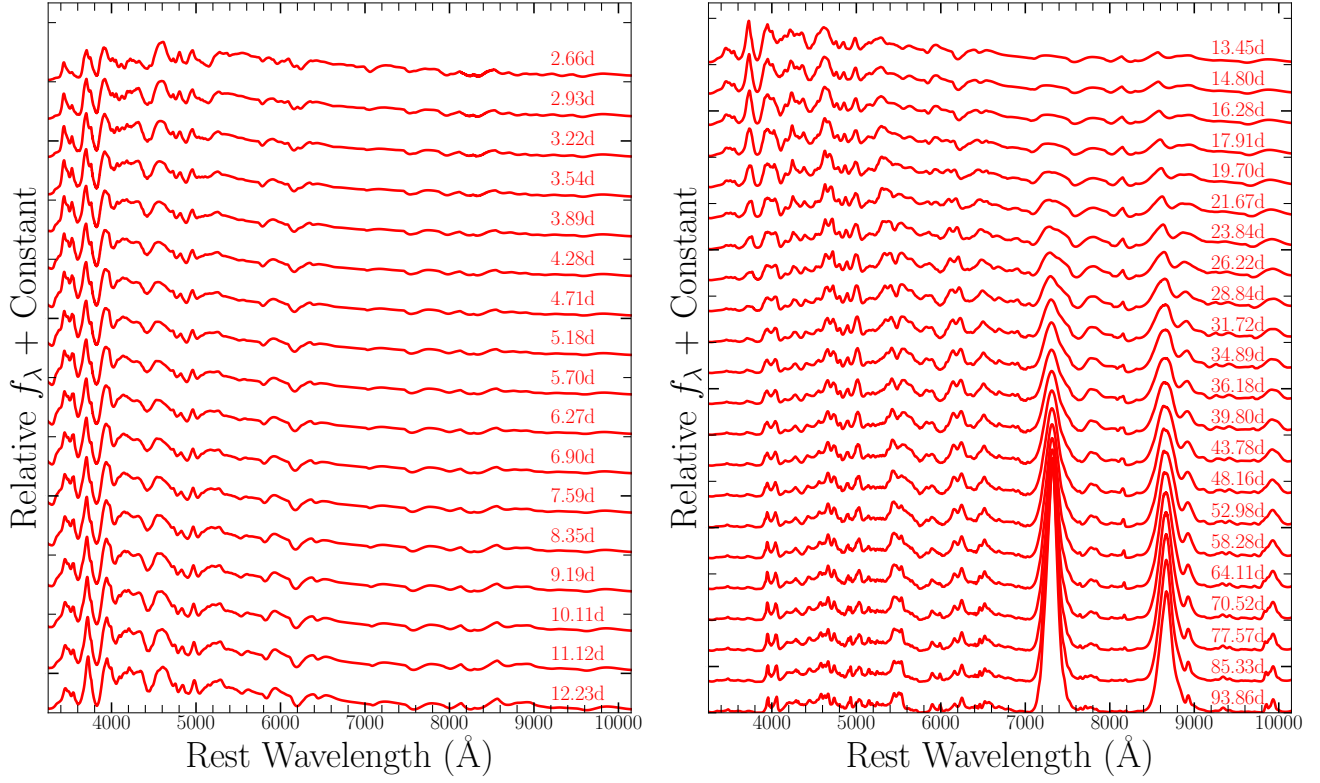


Figure 10. Spectral series of fca_2 model. Each spectrum is normalized by the mean spectral flux.

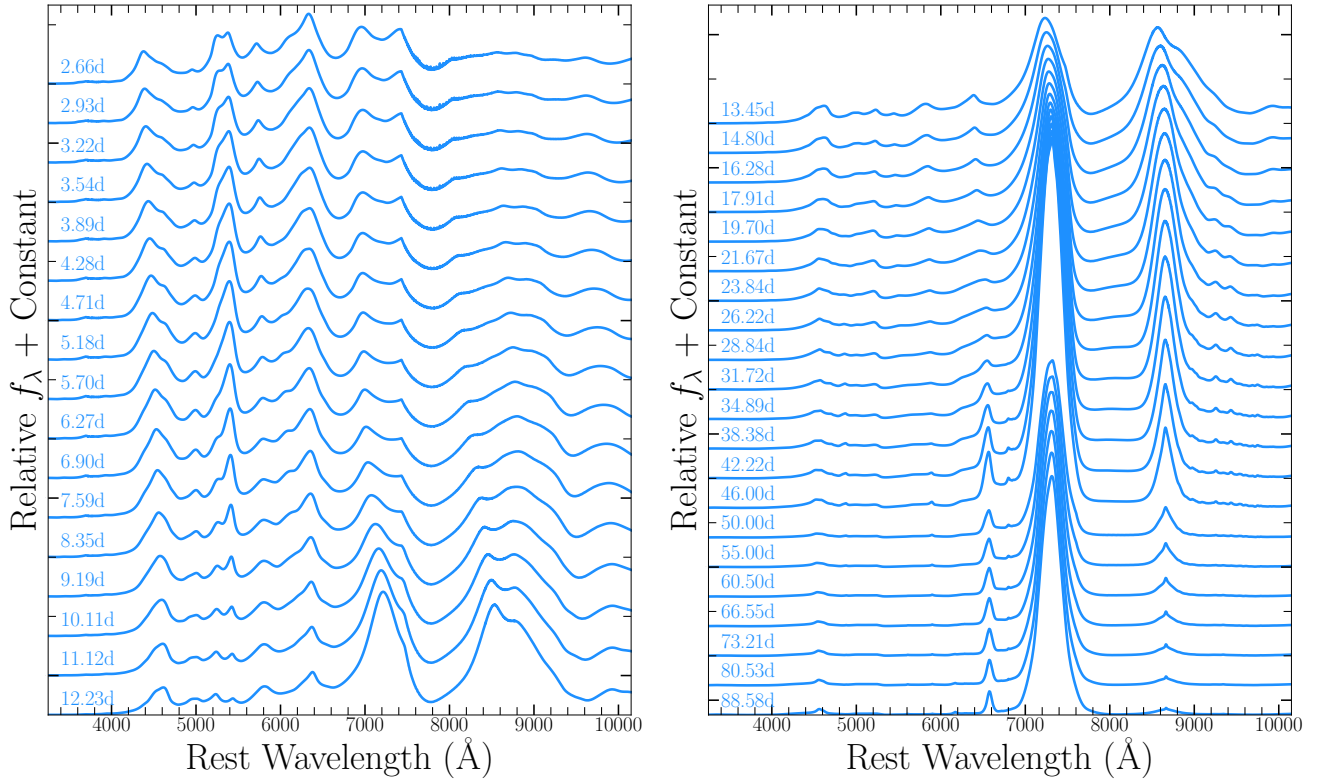


Figure 11. Spectral series of fca_3 model. Each spectrum is normalized by the mean spectral flux.